

LARGE EDDY SIMULATION OF
THREE DIMENSIONAL HIGH SPEED AERODYNAMIC FLOWS

Doyle D. Knight
Dept of Mechanical and Aerospace Engineering
Rutgers - The State University of New Jersey
98 Brett Road
Piscataway, NJ 08854-8058
Telephone: 732 445 4464 · Cellphone: 732 762 5510
Faxsimile: 732 445 4464 · Email: ddknight@rci.rutgers.edu

Final Technical Report
1 Dec 98 - 31 March 02
AFOSR Grant F49620-99-1-0008

Submitted to
Dr. John Schmisser
AFOSR/NM
801 N. Randolph St., Rm 732
Arlington, VA 22203-1977

30 June 2002

20030115 107

REPORT DOCUMENTATION PAGE

JUL -3

1a. REPORT SECURITY CLASSIFICATION Unclassified			1b. RESTRICTIVE MARKINGS Approved for public Distribution unlimited			
2a. SECURITY CLASSIFICATION AUTHORITY			3. DISTRIBUTION STATEMENT			
2b. DECLASSIFICATION/DOWNGRADING SCHEDULE			AFRL-SR-AR-TR-02-			
4. PERFORMING ORGANIZATION REPORT NUMBER(S) RU-TR-MAE-F-203b			5. N 0435			
6a. NAME OF PERFORMING ORGANIZATION Dept. of Mech & Aero Eng Rutgers University		6b. OFFICE SYMBOL (if applicable)		7a. NAME OF MONITORING ORGANIZATION Air Force Office of Scientific Research		
6c. ADDRESS (City, State, and ZIP Code) 98 Brett Road Piscataway, NJ 08854-8058			7b. ADDRESS (City, State, and ZIP Code) 801 N. Randolph Street Arlington, VA 22203-1977			
8a. NAME OF FUNDING/SPONSORING ORGANIZATION Air Force Office of Scientific Research		8b. OFFICE SYMBOL (if applicable)		9. PROCUREMENT INSTRUMENT IDENTIFICATION NUMBER F49620-99-1-0008		
8c. ADDRESS (City, State, and ZIP Code) 801 N. Randolph Street Arlington, VA 22203-1977			10. SOURCE OF FUNDING NUMBERS			
			PROGRAM ELEMENT NO. 2307AS	PROJECT NO.	TASK NO.	
			WORK UNIT ACCESSION NO.			
11. TITLE (Include Security Classification) Large Eddy Simulation of Three Dimensional High Speed Aerodynamic Flows						
12. PERSONAL AUTHOR(S) Doyle Knight						
13a. TYPE OF REPORT Final		13b. TIME COVERED FROM 98/12/01 TO 02/03/31		14. DATE OF REPORT (Year, Month, Day) 02/06/30		
				15. PAGE COUNT 38		
16. SUPPLEMENTARY NOTATION						
17. COSATI CODES			18. SUBJECT TERMS (Continue on reverse if necessary and identify by block number)			
FIELD	GROUP	SUB-GROUP	High speed flows; computational fluid dynamics; turbulence; large eddy simulation; unstructured grids			
19. ABSTRACT (Continue on reverse if necessary and identify by block number)						
<p>An unstructured grid Large Eddy Simulation (LES) methodology has been developed for compressible high speed flows. The filtered compressible Navier-Stokes equations are solved on an unstructured grid of tetrahedra. The inviscid fluxes are obtained from an exact locally one-dimensional Riemann solver using Godunov's method. The viscous fluxes are obtained using a discrete analog of Gauss' Theorem. The reconstruction is performed using a Least Squares technique. The temporal integration is a Runge-Kutta method. The algorithm is overall second order accurate in space and time. Four flowfields have been computed: supersonic flat plate boundary layer, supersonic compression corner, supersonic expansion-compression corner and subsonic square jet. The computed results show close agreement with experiment and Direct Numerical Simulation, and validate the unstructured grid LES methodology.</p>						
20. DISTRIBUTION/AVAILABILITY OF ABSTRACT <input checked="" type="checkbox"/> UNCLASSIFIED/UNLIMITED <input type="checkbox"/> SAME AS RPT. <input type="checkbox"/> DTIC USERS			21. ABSTRACT SECURITY CLASSIFICATION Unclassified			
22a. NAME OF RESPONSIBLE INDIVIDUAL			22b. TELEPHONE (Include Area Code)		22c. OFFICE SYMBOL	

Abstract

An unstructured grid Large Eddy Simulation (LES) methodology has been developed for compressible high speed flows. The filtered compressible Navier-Stokes equations are solved on an unstructured grid of tetrahedra. The inviscid fluxes are obtained from an exact locally one-dimensional Riemann solver using Godunov's method. The viscous fluxes are obtained using a discrete analog of Gauss' Theorem. The reconstruction is performed using a Least Squares technique. The temporal integration is a Runge-Kutta method. The algorithm is overall second order accurate in space and time. Four flowfields have been computed: supersonic flat plate boundary layer, supersonic compression corner, supersonic expansion-compression corner and subsonic square jet. The computed results show close agreement with experiment and Direct Numerical Simulation, and validate the unstructured grid LES methodology.

Table of Contents

Introduction	3
Governing Equations	4
Numerical Algorithm	6
Parallelization	7
Results	7
Supersonic Flat Plate Turbulent Boundary Layer	7
Compression Corner	15
Expansion-Compression Corner	24
Subsonic Square Jet	28
Personnel and Publications	32
Bibliography	34

Introduction

The effective design of high speed aircraft and missiles depends critically upon accurate prediction of aerodynamic and aerothermodynamic performance which are strongly affected by flow turbulence under most flight conditions. From an engineering standpoint, the aircraft or missile aerodynamicist needs the capability for accurate prediction of the mean and rms fluctuating surface pressure (\bar{p}_w and p'_w) and surface heat transfer (\bar{q}_w and q'_w), mean surface skin friction ($\bar{\tau}_w$), and locations of primary and secondary separation.

Table 1: RANS Capability for 3-D Shock Wave Boundary Layer Interaction

<i>Quantity</i>	<i>Satisfactory</i>	<i>Unsatisfactory</i>	<i>No capability shown</i>
\bar{p}_w	✓		
p'_w			✓
\bar{q}_w		✓	
q'_w			✓
Primary Separation	✓		
Secondary Separation		✓	

The current methodology for prediction of compressible turbulent flows is based on the Reynolds-averaged Navier-Stokes (RANS) equations (Knight 1993). This approach has yielded a hierarchy of turbulence models extending from zero-equation to full Reynolds Stress Equation models. While these models have generally been capable of predicting the engineering quantities of interest in weakly perturbed boundary layers, they have been unable to accurately predict the complex 3-D flows which are encountered in highly maneuvering, high angle-of-attack flight. Two recent extensive reviews have documented the capabilities and deficiencies of a wide range of RANS models for prediction of complex 3-D flows with shock wave-turbulent boundary layer interactions (Knight 1997, Knight and Degrez 1998). The results, summarized in Table 1, indicate that a significant number of critical engineering quantities are not capable of prediction by current RANS models. Therefore, more advanced turbulence models are needed which have the ability to simulate the complex physics of turbulence with greater generality.

Large Eddy Simulation (LES) is an alternative to RANS which may be capable of predicting more (or all) of the aerodynamic and aerothermodynamic quantities of engineering interest described above. In LES, the governing equations are spatially filtered on the scale of the numerical grid. The large, energy-containing eddies are directly computed. These eddies are strongly influenced by the physical geometry and configuration of the flow. Thus, the direct computation of the large eddies by LES, as opposed to the modeling of the large eddies by RANS, gives greater generality, in principle, to LES. The influence of the unresolved scales of motion is simulated using a subgrid-scale (SGS) model (Smagorinsky 1963, Lilly 1967, Deardorff 1970, Germano *et al* 1991, Piomelli *et al* 1991, Ghosal *et al* 1995) or by the inherent dissipation in the numerical scheme (Boris *et al* 1992, Oran and Boris 1993, Porter *et al* 1994, Grinstein 1996, Ansari and Strang 1996). Because the statistics of the small scale turbulence are expected to be more homogeneous and isotropic than those of the large scales, a general model of the small scales seems more plausible than a general model of the entire spectrum of turbulent motions.

LES has been shown to be both a useful research tool for understanding the physics of turbulence, and also a predictive method for flows of engineering interest. Recent compendia and reviews include Galperin and Orszag (1993), Mason (1994), Lesieur and Métais (1996) and Moin (1997).

Many models have been developed for the subgrid-scale stress tensor. These include the conventional Smagorinsky eddy viscosity model (Smagorinsky 1963, Lilly 1967, Deardorff 1970), the spectra eddy viscosity model of Kraichnan (1976), the dynamic SGS model of Germano *et al* (1991), the scale similarity model of Bardina *et al* (1980), and the localized dynamic SGS model of Ghosal *et al* (1995) and more recently of Menon and Kim (1996), and many others. Although most research has focused on incompressible turbulent flows, there has recently emerged a growing interest in applications of LES to compressible turbulent flows. Examples include Yoshizawa (1986), Speziale *et al* (1988), Moin *et al* (1991), Erlebacher *et al* (1992), Zang *et al* (1992), El-Hady *et al* (1994), Jansen (1997), Spyropoulos and Blaisdell (1996), and Haworth and Jansen (1996). Nearly all compressible LES has employed spectral methods or structured grids, with the exception of Jansen and Haworth.

Apart from the complexities of the flowfield, the complicated geometries of high speed vehicles is also a challenge. To enable treatment of complex geometries and also achieve high resolution of the flowfield dynamically, we employ an unstructured grid. There are two important advantages of unstructured grids. First, algorithms have been developed to facilitate automatic generation of unstructured grids for a complex geometries (see, for example, the discussion in Barth (1990, 1992). These grid generation methods can be substantially more efficient (in terms of user time) than some of the multi-block structured grid generation methods used. Second, local mesh refinement, either adaptive or fixed, can be performed much more readily for unstructured grids.

The report summarizes the research in Large Eddy Simulation of compressible turbulent flows using unstructured grids. Two methods for simulation of the subgrid scale stresses have been examined. The first method is the Monotone Integrated Large Eddy Simulation (MILES) technique. The second method is a hybrid technique combining MILES with a Smagorinsky eddy viscosity model for the subgrid scale stresses. These two methods, together with different algorithms for the inviscid fluxes and function reconstruction, have been evaluated for four turbulent flows: supersonic boundary layer, supersonic compression corner, supersonic expansion-compression corner and subsonic square jet. The results are in overall good agreement with the experiment and Direct Numerical Simulation (DNS), thereby validating the accuracy of the methodology.

Governing Equations

The governing equations are the three-dimensional filtered Navier-Stokes equations. For a function f , its filtered form \bar{f} is

$$\bar{f} \equiv \frac{1}{V} \int_V G f dV$$

where G is the filtering function, and its Favre-averaged form \tilde{f} is

$$\tilde{f} \equiv \frac{\bar{\rho f}}{\bar{\rho}}$$

where ρ is the density. From the Navier-Stokes equations for the instantaneous flow variables density (ρ), velocity in the i th coordinate direction (u_i), pressure (p) and temperature (T), Favre-averaging and spatial filtering yield the filtered Navier-Stokes equations (here written using the Einstein summation notation where repeated indices denote summation)

$$\begin{aligned} \frac{\partial \bar{\rho}}{\partial t} + \frac{\partial \bar{\rho} \tilde{u}_k}{\partial x_k} &= 0 \\ \frac{\partial \bar{\rho} \tilde{u}_i}{\partial t} + \frac{\partial \bar{\rho} \tilde{u}_i \tilde{u}_k}{\partial x_k} &= -\frac{\partial \bar{p}}{\partial x_i} + \frac{\partial \bar{\tau}_{ik}}{\partial x_k} \end{aligned}$$

$$\begin{aligned}\frac{\partial \bar{\rho} \tilde{e}}{\partial t} + \frac{\partial}{\partial x_k} (\bar{\rho} \tilde{e} + \bar{p}) \tilde{u}_k &= \frac{\partial Q_k}{\partial x_k} + \frac{\partial}{\partial x_k} (\mathcal{T}_{ik} \tilde{u}_i) \\ \bar{p} &= \bar{\rho} R \tilde{T}\end{aligned}$$

where

$$\begin{aligned}\mathcal{T}_{ik} &= \tau_{ik} + \bar{\sigma}_{ik} \\ \tau_{ik} &= -\bar{\rho} (\tilde{u}_i \tilde{u}_k - \tilde{u}_i \tilde{u}_k) \\ \bar{\sigma}_{ik} &= \mu(\tilde{T}) \left(-\frac{2}{3} \frac{\partial \tilde{u}_j}{\partial \tilde{x}_j} \delta_{ik} + \frac{\partial \tilde{u}_i}{\partial x_k} + \frac{\partial \tilde{u}_k}{\partial x_i} \right) \\ Q_k &= Q_k + \bar{q}_k \\ Q_k &= -\bar{\rho} c_p (\tilde{T} \tilde{u}_k - \tilde{T} \tilde{u}_k) \\ \bar{q}_k &= k(\tilde{T}) \frac{\partial \tilde{T}}{\partial x_k} \\ \bar{\rho} \tilde{e} &= \bar{\rho} c_v \tilde{T} + \frac{1}{2} \bar{\rho} \tilde{u}_i \tilde{u}_i + \bar{\rho} \tilde{k} \\ \bar{\rho} \tilde{k} &= \frac{1}{2} (\bar{\rho} \tilde{u}_i \tilde{u}_i - \bar{\rho} \tilde{u}_i \tilde{u}_i) = -\frac{1}{2} \tau_{ii}\end{aligned}$$

Two different Sub-Grid-Scale (SGS) models are employed. The first model is Monotone Integrated Large Eddy Simulation (MILES) wherein the numerical algorithm itself provides the requisite dissipation associated with the subgrid scale motions. The second model is the classical constant-coefficient Smagorinsky method

$$\begin{aligned}\tilde{S}_{ij} &= \frac{1}{2} \left(\frac{\partial \tilde{u}_i}{\partial \tilde{x}_j} + \frac{\partial \tilde{u}_j}{\partial \tilde{x}_i} \right) \\ \tau_{ij} &= 2C_R \bar{\rho} \Delta^2 \sqrt{\tilde{S}_{mn} \tilde{S}_{mn}} \left(\tilde{S}_{ij} - \frac{1}{3} \tilde{S}_{kk} \delta_{ij} \right) \\ Q_j &= \bar{\rho} c_p \frac{C_R}{Pr_t} \Delta^2 \sqrt{\tilde{S}_{mn} \tilde{S}_{mn}} \frac{\partial \tilde{T}}{\partial x_j}\end{aligned}$$

where $C_R = 0.00423$ and Δ is the length scale which is related to the local grid size. For boundary layer flows, Δ is multiplied by the Van Driest damping factor

$$D = 1 - e^{-n^+/A}$$

where $A = 26$, $n^+ = n u_\tau / \nu_w$ is the normal distance to the (nearest) solid boundary normalized by the viscous length scale ν_w / u_τ where ν_w is the kinematic viscosity evaluated at the wall and U_τ is the local friction velocity.

We simplify the notation by hereafter dropping the tilde \sim and overbar $\bar{\cdot}$. The flow variables are nondimensionalized using the reference density ρ_∞ , velocity U_∞ , static temperature T_∞ and length scale L , with Mach number $M_\infty = U_\infty / \sqrt{\gamma R T_\infty}$. The governing equations are therefore

$$\frac{\partial \rho}{\partial t} + \frac{\partial \rho u_k}{\partial x_k} = 0$$

$$\begin{aligned}
\frac{\partial \rho u_i}{\partial t} + \frac{\partial \rho u_i u_k}{\partial x_k} &= -\frac{\partial p}{\partial x_i} + \frac{\partial \mathcal{T}_{ik}}{\partial x_k} \\
\frac{\partial \rho e}{\partial t} + \frac{\partial}{\partial x_k} (\rho e + p) u_k &= \frac{\partial}{\partial x_k} (Q_k + \mathcal{T}_{ik} u_i) \\
p &= \frac{\rho T}{\gamma M_\infty^2}
\end{aligned}$$

Numerical Algorithm

The governing equations are expressed in finite volume form for a control volume V with surface ∂V

$$\frac{d}{dt} \int_V Q dV + \int_{\partial V} (F\hat{i} + G\hat{j} + H\hat{k}) \cdot \hat{n} dA = 0$$

where Q is the vector of dependent variables

$$Q = \begin{pmatrix} \rho \\ \rho u \\ \rho v \\ \rho w \\ \rho e \end{pmatrix}$$

and the flux vectors are

$$F = \begin{pmatrix} \rho u \\ \rho u^2 + p - \mathcal{T}_{xx} \\ \rho uv - \mathcal{T}_{xy} \\ \rho uw - \mathcal{T}_{xz} \\ (\rho e + p)u - Q_x - \beta_x \end{pmatrix}, \quad G = \begin{pmatrix} \rho v \\ \rho uv - \mathcal{T}_{xy} \\ \rho v^2 + p - \mathcal{T}_{yy} \\ \rho vw - \mathcal{T}_{yz} \\ (\rho e + p)v - Q_y - \beta_y \end{pmatrix}, \quad H = \begin{pmatrix} \rho w \\ \rho vw - \mathcal{T}_{yz} \\ \rho w^2 + p - \mathcal{T}_{zz} \\ (\rho e + p)w - Q_z - \beta_z \end{pmatrix}$$

with

$$\begin{aligned}
\beta_x &= \mathcal{T}_{xx}u + \mathcal{T}_{xy}v + \mathcal{T}_{xz}w \\
\beta_y &= \mathcal{T}_{xy}u + \mathcal{T}_{yy}v + \mathcal{T}_{yz}w \\
\beta_z &= \mathcal{T}_{xz}u + \mathcal{T}_{yz}v + \mathcal{T}_{zz}w
\end{aligned}$$

An unstructured grid of tetrahedra is employed, with a cell-centered storage architecture. The cell-averaged values, stored at the centroid of each tetrahedron of volume V_i are

$$Q_i = \frac{1}{V_i} \int_{V_i} Q dV$$

The inviscid fluxes are computed using Godunov's method which is an exact one-dimensional Riemann solver (Gottlieb and Groth 1988) applied normal to each face. The inviscid flux computations require the values of each variable on either side of the cell faces. These values are obtained from the cell-averaged values by second-order or third-order function reconstruction using the Least Squares

method of Ollivier-Gooch (Ollivier-Gooch 1997). The second-order function reconstruction method of Frink (1994) was employed in some of the earlier LES studies, but was found inferior to the method of Ollivier-Gooch (Okong'o and Knight 1998). More details on the reconstruction schemes are given in Okong'o and Knight (1998).

The viscous fluxes and heat transfer are computed by application of Gauss' theorem to the control volume whose vertices are the centroids of the cells which share each node. The second-order accurate scheme (in 2-D) is given by Knight (1994) and the extension to 3-D is straightforward.

Parallelization

The code is parallelized using domain decomposition and Message Passing Interface (MPI). Domain decomposition is performed in a pre-processing step. The domain is decomposed in a single direction with equal number of tetrahedra in each domain. A halo of cells is added in each domain to provide data on the adjacent domain, and the halo cell data is updated at every subiterate of the time integration. An example is shown in Fig. 1 for the LES of decay of isotropic turbulence. The numerical algorithm achieves excellent parallel performance. For example, the speed-up on four processors of the SGI Power Onyx with R-10000 processors is 3.7 for 93% efficiency (Knight *et al* 1998).

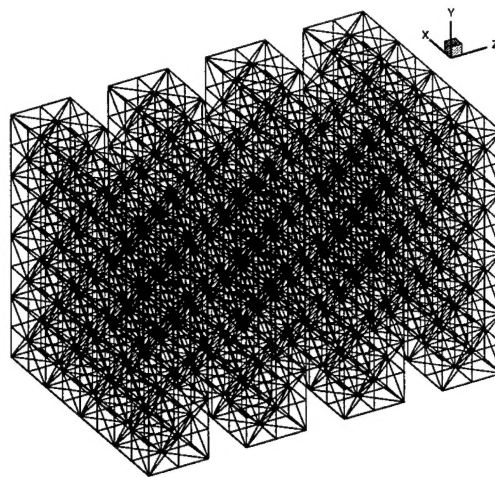


Figure 1: Example of domain decomposition

Results

Four different configurations have been examined: supersonic flat plate boundary layer, supersonic compression corner, expansion-compression corner and subsonic square jet.

1 Supersonic Flat Plate Turbulent Boundary Layer

The adiabatic and isothermal flat plate turbulent boundary layers at Mach 3 and Mach 4 at Reynolds number $Re_\delta = 2 \times 10^4$ (based on the incoming boundary layer thickness δ) have been computed. The Reynolds number based on the momentum thickness δ_2 and wall viscosity μ_w is $Re_{\delta_2} = 600$. The Reynolds number is sufficiently high to achieve turbulent flow.

The inflow conditions are obtained using a compressible extension of the method of Lund *et al* (1998). The simulation generates its own inflow conditions through a sequence of operations where the velocity field at a downstream station is rescaled and reintroduced at the inflow boundary (Fig. 2). Defining x, y and z to denote the streamwise, transverse and spanwise directions, respectively, the size of the computational domain is $L_x = 14.8\delta$, $L_y = 3.4\delta$ and $L_z = 2.0\delta$. The spanwise width L_z is approximately three times the experimental spanwise streak spacing (assuming the compressible turbulent boundary layer streaks scale in accordance with incompressible experimental results). The streamwise length L_x is approximately three times the mean experimen-

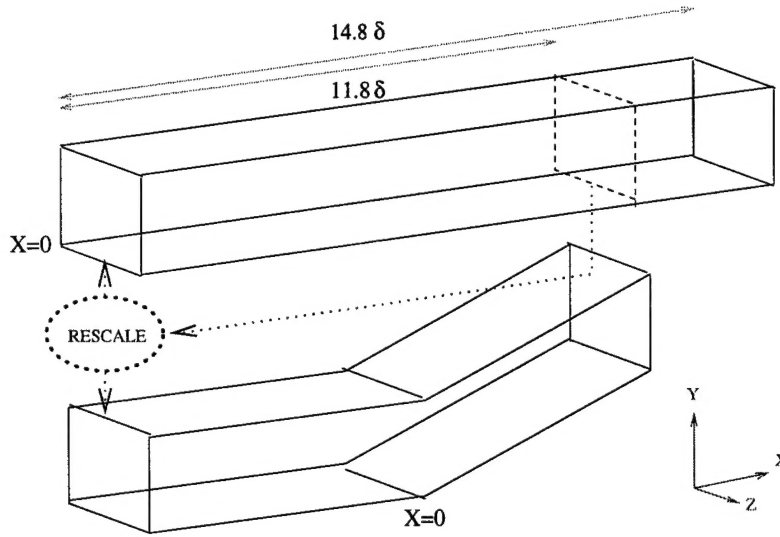


Figure 2: Computational domain

tal streamwise streak size. The height L_y is based on the requirement that acoustic disturbances originating at the upper boundary do not interact with the boundary layer on the lower wall.

The reference quantities for non-dimensionalization are the incoming boundary layer thickness δ , velocity U_∞ , density ρ_∞ , static temperature T_∞ and molecular viscosity μ_∞ (where the subscript ∞ denotes the freestream condition). The grid resolution near the wall is dependent on Δx^+ , Δy^+ and Δz^+ , where $\Delta x^+ = \Delta x/\eta$, $\Delta y^+ = \Delta y/\eta$ and $\Delta z^+ = \Delta z/\eta$. The inner length scale is $\eta = \nu_w/u_\tau$, where ν_w is the kinematic viscosity at the wall, $u_\tau = \sqrt{\tau_w/\rho_w}$ is the friction velocity, τ_w is the wall shear stress and ρ_w is the density at the wall. Before we proceed with the discussion about the grid resolution, we first describe how to obtain η .

The theoretical value of the friction velocity u_τ for a supersonic flat plate boundary is obtained from the combined Law of the Wall and Wake evaluated at $y = \delta$

$$\frac{U_{VD}}{u_\tau} = \frac{1}{\kappa} \ln(y \frac{u_\tau}{\nu_w}) + C + \frac{2\Pi}{\kappa} \sin^2(\frac{\pi y}{2\delta}) \quad (1)$$

where

$$U_{VD} = \frac{U_\infty}{A} \left\{ \sin^{-1} \left[\frac{2A^2(\frac{U}{U_\infty}) - B}{\sqrt{B^2 + 4A^2}} \right] + \sin^{-1} \left[\frac{B}{\sqrt{B^2 + 4A^2}} \right] \right\} \quad (2)$$

$$\nu_w = \nu_\infty \left(\frac{T_w}{T_\infty} \right)^{1+\omega}$$

$$A = \left(\frac{\gamma-1}{2} Pr_{tm} M_\infty^2 \frac{T_\infty}{T_w} \right)^{1/2}$$

$$B = \frac{T_{aw}}{T_w} - 1$$

$$T_{aw} = T_\infty \left[1 + \frac{(\gamma-1)}{2} Pr_{tm} M_\infty^2 \right]$$

where $\kappa = 0.4$ is von Karman's constant, $C = 5.1$, the wake parameter Π is 0.12 at $Re_\delta = 2 \times 10^4$, the exponent ω is 0.76, the mean turbulent Prandtl number Pr_{tm} is 0.89 and the ratio of specific

heats γ is 1.4. The wall temperature T_w is fixed at 10% above the theoretical adiabatic temperature T_{aw} for the isothermal boundary. In the computation, u_τ and ν_w are obtained from $u_\tau = \sqrt{\tau_w/\rho_w}$ and $\nu_w = \nu_\infty (\frac{T_w}{T_\infty})^{1+\omega}$, respectively.

The variation of Mach number and the different temperature boundary condition have effect on η , therefore on Δx^+ , Δy^+ and Δz^+ . At the same Mach number, the wall temperature for the isothermal case is 10% higher than that for the adiabatic case, leading to the larger η and the smaller Δx^+ if keeping the same Δx . However this effect is very small in our case, therefore we keep the same Δx , Δy and Δz for the different temperature condition at the same Mach number. The grid details are shown in Table 2.

Table 2: Details of Grid

	A3	I3	A4	I4
Δx^+	20	18	12	11
Δy^+	1.8	1.6	1.8	1.6
Δz^+	7	6.4	4	3.4
$\Delta x/\delta$	0.1	0.1	0.1	0.1
$\Delta y/\delta$	0.18	0.18	0.18	0.18
$\Delta z/\delta$	0.034	0.034	0.034	0.034

where A and I stand for the adiabatic and isothermal cases, respectively and the number followed indicates the Mach number. The Δx^+ , Δy^+ and Δz^+ are measured at the wall and the Δx , Δy and Δz are measured at $y/\delta = 1.0$. The grid is uniform in x and z directions and stretched in y direction with about 23 layers of tetrahedra in the boundary layer for each case.

The initial condition is a turbulent mean profile with random fluctuations. The simulation is run first for 90 inertial timescales δ/U_∞ in order to eliminate starting transients (Lund *et al* 1998).

For a function f , its average in time form $\langle f \rangle$ is defined by

$$\langle f \rangle = \frac{1}{t_f - t_i} \int_{t_i}^{t_f} f dt$$

and its time fluctuating part is

$$f'' = f - \langle f \rangle$$

In order to provide converged data, the primitive variables are averaged in spanwise direction and the statistical evaluations are performed on a period longer than $t_f - t_i = 40\delta/U_\infty$. The notation for the combined temporal and spanwise average is

$$\langle\langle f \rangle\rangle = \frac{1}{L_z} \frac{1}{t_f - t_i} \int_0^{L_z} \int_{t_i}^{t_f} f dt dz$$

A simplifying notation is used for the velocity, temperature and pressure

$$U = \langle\langle u \rangle\rangle$$

The mean streamwise velocity profiles using the Van Driest transformation are plotted in Fig. 3 and Fig. 4 (where u_τ is obtained from the simulation). Good agreement is shown with the viscous sublayer linear approximation $U_{VD}/u_\tau = y^+$ and Law of the Wall formulated in (1).

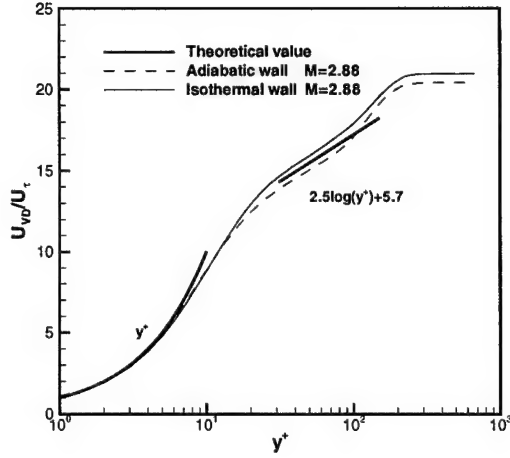


Figure 3: Van Driest velocity at M=3

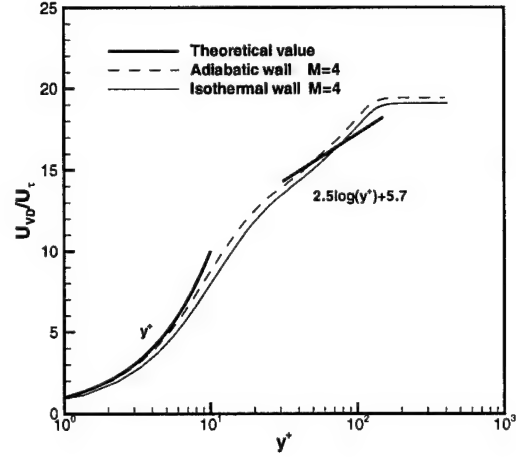


Figure 4: Van Driest velocity at M=4

The mean velocity profiles shown in Fig. 5 and Fig. 6 exhibit virtually identical distributions for adiabatic and isothermal cases and show good agreement with experiment (Zheltonovodov *et al* 1986, Zheltovodov *et al* 1990). The mean temperature profiles in Fig. 7 and Fig. 8 display a higher temperature distribution for the isothermal case with the wall temperature higher than the adiabatic and experiment data (Zheltonovodov *et al* 1990) which are also obtained at the adiabatic boundary condition. The difference is expected since the wall temperature for the isothermal case is fixed at 10% higher than the adiabatic case.

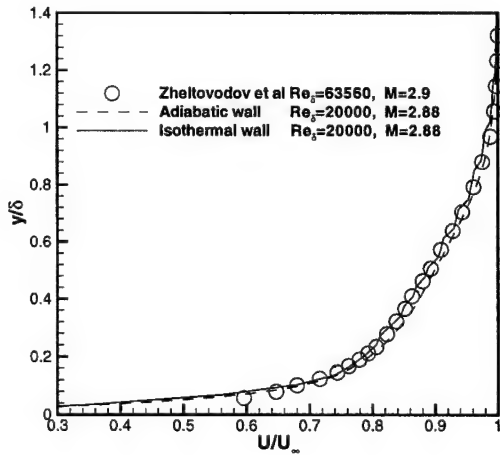


Figure 5: Streamwise velocity at M=3

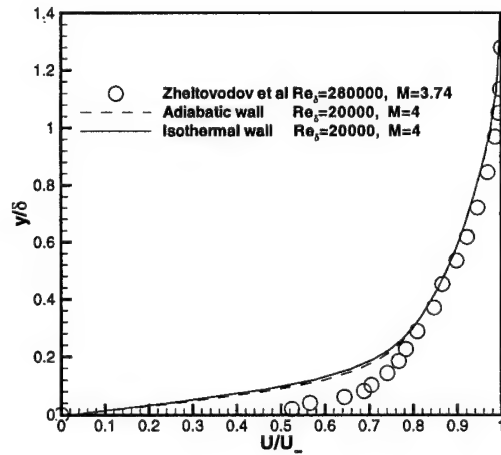


Figure 6: Streamwise velocity at M=4

The discrepancies between Mach 4 cases and experiments in Fig. 6 and Fig. 8 are due to the effects of Mach number and Reynolds number. The Reynolds number in the simulation is one magnitude lower than experiments due to the significant computation cost in LES. The outer portion of the velocity profiles in Fig. 6 is in good agreement with experiment since this portion is not sensitive to the Reynolds number. The discrepancy in the inner portion is due to the effect of the Reynolds

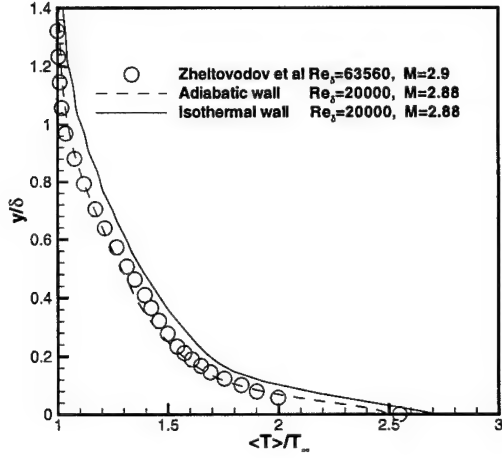


Figure 7: Temperature at M=3

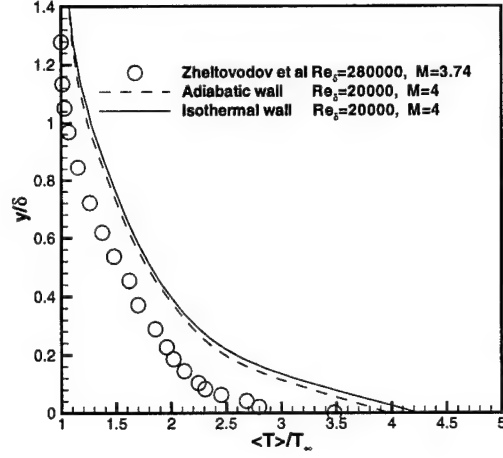


Figure 8: Temperature at M=4

number. The effect of Mach number is observed in Fig. 8, which can be explained using Crocco's relationship between the mean temperature and mean velocity profiles

$$\frac{T}{T_\infty} = \frac{T_w}{T_\infty} + \frac{T_{aw} - T_w}{T_\infty} \frac{U}{U_\infty} - r \frac{\gamma - 1}{2} M_\infty^2 \left(\frac{U}{U_\infty} \right)^2 \quad (3)$$

where r is the recovery factor defined as

$$r = \frac{T_r - T_\infty}{T_0 - T_\infty} \quad (4)$$

where T_r is the adiabatic or recovery temperature and T_0 is the freestream stagnation temperature. For the adiabatic case, Eq. (3) becomes

$$\frac{T}{T_\infty} = \frac{T_w}{T_\infty} - r \frac{\gamma - 1}{2} M_\infty^2 \left(\frac{U}{U_\infty} \right)^2 \quad (5)$$

Eqs. (3) and (5) show the trend that under the same mean velocity distribution, the mean temperature decreases with increasing Mach number, leading to the discrepancy between the calculation and experiment in the outer portion of the mean temperature profiles in Fig. 8. The discrepancy in the inner portion is mainly due to the effect of the Reynolds number.

The mean streamwise resolved turbulent kinematic normal stress $\langle\langle u''u'' \rangle\rangle$, normalized using the local mean density $\langle\langle \rho \rangle\rangle$ and wall shear stress τ_w , is shown in Fig. 9 and Fig. 10. As discussed in Zheltovodov and Yakovlev (1986) and Smits and Dussauge (1996), the scaling $\langle\langle \rho \rangle\rangle \langle\langle u''u'' \rangle\rangle / \tau_w$ provides an approximate self-similar correlation of experimental data for supersonic flat plate zero pressure gradient adiabatic boundary layers, although the measurements close to the wall are subject to considerable uncertainty. In those two figures data are displayed from Konrad and Smits (1998), Johnson and Rose (1975), Muck *et al* (1984, 1985), Konrad (1993), as well as upper and lower bounds of an extensive set of experimental data for the Mach number range $M = 1.72$ to 9.4 in accordance with generalizations of Zheltovodov and Yakovlev (1986). The characteristics of the different experiments are displayed in Table 3. The computed results show good agreement with experiment for the main part of the boundary layer ($y/\delta > 0.2$), despite a significantly higher

Table 3: Flat Plate Boundary Layer Experimental Data

Name	Mach No.	Re_δ
LES	3.0 & 4.0	20×10^3
DNS Adams (1997)	3.0	25×10^3
Johnson & Rose (1975)	2.9	1000×10^3
Konrad (1993)	2.9	1590×10^3
Konrad & Smits (1998)	2.87	1900×10^3
Muck <i>et al</i> (1984, 1985)	2.87	1638×10^3
Zhel'tovodov <i>et al</i> (1986)	1.7-9.4	up to 2000×10^3

experimental Reynolds number. The decreasing slope corresponds precisely to Johnson and Rose (1975) data. For $y/\delta < 0.2$ the presence of the typical high level peak in the near wall region is supported by experimental data of Konrad (1993) and the Direct Numerical Simulation data from Adams (1997), which is nearly at the same Reynolds number as the LES. However, no conclusion can be drawn about the precise y position and the width of this peak without further experimental data or DNS.

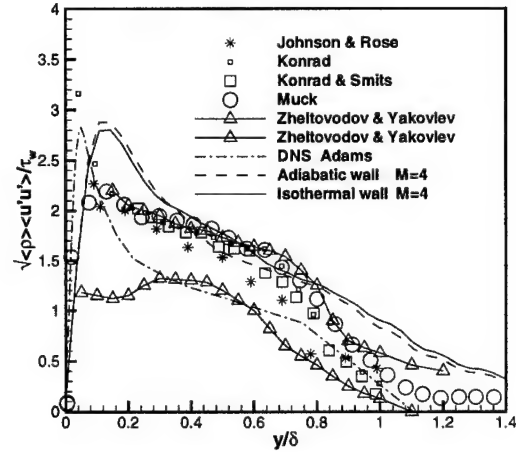
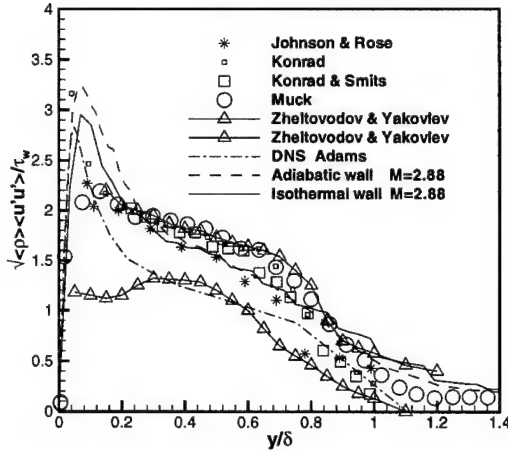


Figure 9: Streamwise Reynolds stress at M=3 Figure 10: Streamwise Reynolds stress at M=4

In Fig. 11 and Fig. 12 Reynolds shear stress distributions are shown for the same experiments and the DNS. Again, the data fit well in the outer part of the boundary layer. The maximum value and the decreasing slope are again well predicted.

The capability of our LES method to accurately predict the heat transfer in the flat plate boundary layer is evaluated. The Reynolds analogy relates the skin friction coefficient C_f and heat transfer coefficient C_h by the Prandtl number as follows

$$\frac{2C_h}{C_f} = \frac{1}{Pr_{tm}} \quad (6)$$

where C_h and C_f are written as

$$C_h = \frac{q_w}{\rho_\infty U_\infty c_p (T_w - T_{aw})} \quad (7)$$

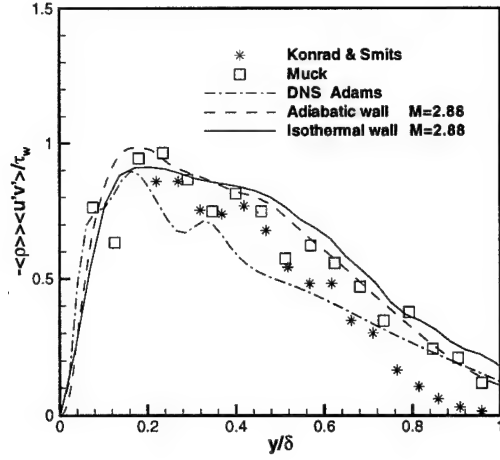


Figure 11: Reynolds shear stress at M=3

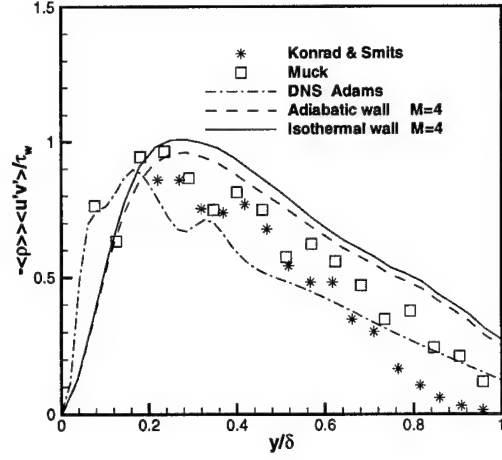


Figure 12: Reynolds shear stress at M=4

$$C_f = \frac{\tau_w}{\frac{1}{2} \rho_\infty U_\infty^2} \quad (8)$$

where c_p is the specific heat at constant pressure. The wall heat flux (q_w) and skin friction (τ_w) are obtained from the isothermal case and the adiabatic wall temperature (T_{aw}) is calculated from the adiabatic case. The wall heat flux is

$$q_w = -\lambda \frac{\partial T}{\partial y} \Big|_w \quad (9)$$

and the wall shear stress is

$$\tau_w = \mu_w \frac{\partial u}{\partial y} \Big|_w \quad (10)$$

Table 4: LES predictions

Name	T_w/T_∞	C_f	C_h
A2.88	2.51	2.44×10^{-3}	0
I2.88	2.72	2.32×10^{-3}	1.27×10^{-3}
A4	3.95	1.97×10^{-3}	0
I4	4.23	2.00×10^{-3}	1.24×10^{-3}

Table 5: Comparison of LES and Experiment

Cases	Name	LES	Experiment	Error
Mach=2.88	T_{aw}/T_∞	2.51	2.549	1.5%
	C_f	2.32×10^{-3}	2.56×10^{-3}	9.4%
	C_h	1.27×10^{-3}	1.44×10^{-3}	11.8%
	$2C_h/C_f$	1/0.91	1/0.89	2.2%
	Pr_{tm}	0.91	0.89	2.2%
Mach=4.0	T_{aw}/T_∞	3.95	3.848	2.6%
	C_f	2.0×10^{-3}	2.17×10^{-3}	7.8%
	C_h	1.24×10^{-3}	1.22×10^{-3}	1.6%
	$2C_h/C_f$	1/0.81	1/0.89	9.9%
	Pr_{tm}	0.81	0.89	9.0%

Note:

Experimental T_{aw} from Eq. (3)

Experimental C_f from Eqs. (1), (2) and (8)

Experimental C_h from Eq. (6)

The wall temperature T_w is fixed at $T_w = 1.1T_{aw}$, where the empirical adiabatic wall temperature $T_{aw} = [1 + \frac{(\gamma-1)}{2}Pr_{tm}M_\infty^2]T_\infty$. All the predicted results are listed in Table 4, where the wall temperature for the isothermal case is fixed. The comparison with experiment is shown in Table 5. The experimental adiabatic wall temperature is computed from $T_{aw} = [1 + \frac{(\gamma-1)}{2}Pr_{tm}M_\infty^2]T_\infty$. The computed mean turbulent Prandtl number from (6) shows good agreement with experiment value of 0.89, indicating the consistency of LES results with the Reynolds analogy.

The turbulent Prandtl number changes across the boundary layer. Simpson *et al* (1970) have established the uncertainty envelope of the turbulent Prandtl number for incompressible zero pressure gradient turbulent boundaries. The experimental predictions by Meier and Rotta (1971) at Mach number up to 4.5 at the wall and Horstman and Owen (1972) at $M=7.2$ and cooled wall conditions fall into this uncertainty envelope. According to the eddy viscosity hypothesis, the turbulent stress and heat flux can be expressed as

$$\tau_{ik} = -\overline{\rho u'_i u'_k} = \mu_t \left(\frac{\partial \tilde{u}_i}{\partial x_k} + \frac{\partial \tilde{u}_k}{\partial x_i} - \frac{2}{3} \frac{\partial \tilde{u}_j}{\partial x_j} \delta_{ik} \right) - \frac{2}{3} \tilde{\rho} \tilde{k} \delta_{ik} \quad (11)$$

$$Q_k = -c_p \overline{\rho T' u'_k} = \lambda \frac{\partial \tilde{T}}{\partial x_k} \quad (12)$$

where the bar $\overline{}$ denotes the filtered flow variables and the tilde $\tilde{}$ denotes the Favre-averaged filtered flow variables. The local turbulent Prandtl number (Pr_t) for a two-dimensional boundary layer can be derived from the above two equations as

$$Pr_t = \frac{\frac{\partial \tilde{T}}{\partial y} \overline{\rho u' v'}}{\frac{\partial \tilde{u}}{\partial y} \overline{\rho T' v'}} \quad (13)$$

The calculated turbulent Prandtl number profile is shown compared with the experimental range in Fig. 13. The Prandtl number reaches the maximum at the wall and starts to decrease away from the wall. In the outer portion of boundary layer, the fluctuation of Prandtl number is relatively greater than the inner portion, which is consistent with the experimental trend.

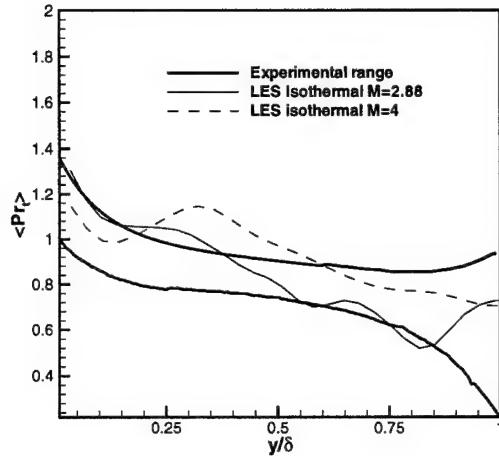


Figure 13: Turbulent Prandtl number

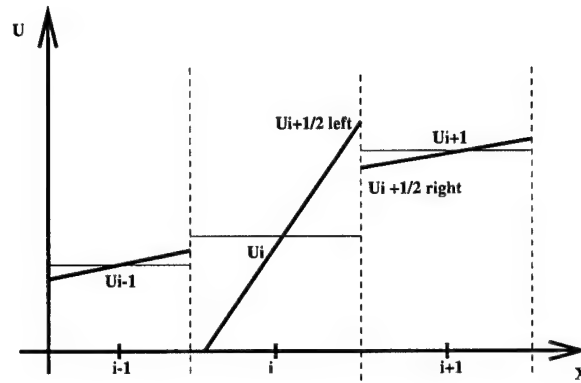


Figure 14: Example of overshoot

2 Compression Corner

Supersonic flow past a compression corner is an important problem in aerodynamics. It represents, for example, the deflection of a control surface on a wing. The shock can cause a boundary layer separation upstream of the point of impingement of the primary shock, with a secondary shock forming near the separation (Andreopoulos and Muck 1987, Dolling and Or 1983, Horstman *et al* 1977, Settles *et al* 1979, Smits and Muck 1987, Zheltovodov *et al* 1983, Zheltovodov and Yakolev 1986, and Zheltovodov 1996). Reynolds-averaged Navier-Stokes simulations have failed to accurately predict the flow characteristics (Knight and Degrez 1998) such as fluctuating pressure and heat transfer.

2.1 Weighting Function and Limiters

The computation of a strong shock using the exact Riemann solver (Godunov's method) and the Least Squares method (Ollivier 1997) as a reconstruction scheme leads to the generation of oscillations in the vicinity of shock waves which cause numerical instability. It can be shown theoretically that a linear second-order upwind scheme always generates oscillations. The only way to overcome this limitation, while satisfying the concept of an entropy function, is to introduce non-linear components. The classical method to avoid such spurious oscillations is to implement limiters which control the gradient of the computed quantities to prevent the appearance of overshoots and undershoots. An excellent review of this technique is described in Hirsh 1997. A different approach is the stencils-searching ENO schemes which have been extended to unstructured grids (Abgrall 1994). At each time step, the stencil is chosen which provides the smoothest reconstruction. However, this approach is computationally expensive for LES since it implies a determination of the stencil at every time step. Recently, Ollivier-Gooch (Ollivier 1997) proposed a weighted stencil method wherein the stencil is fixed but the weights are recomputed at each time step as required¹.

¹We found that the weighted stencil method of Ollivier-Gooch (Ollivier 1997) provided an improvement compared to the unweighted results, but was nonetheless very sensitive to the weighting parameters. For the 25° compression corner, we found that overshoots and undershoots in the vicinity of the shock could not be avoided without adversely

2.2 Limiters

We consider limiters which control the gradient of computed quantities reconstructed to a cell face (denoted by the index $i + \frac{1}{2}$). The limiters described in the literature (*e.g.*, Van Leer's limiter, Minmod, Roe's Superbee limiter) are expressed as a function of the ratio $r_{i+\frac{1}{2}}$ of consecutive variations

$$r_{i+\frac{1}{2}} = \frac{u_{i+1} - u_i}{u_i - u_{i-1}} \quad (14)$$

This expression is well defined in case of a structured grid, where $i + 1$ means the next cell in the i discretization and $i - 1$ means the previous one.

2.3 Homogeneous Limiter

Consider a linear reconstruction of a flow variable wherein the computed gradient yields an overshoot (or undershoot) in the reconstructed value at the cell interface (Fig. 14). The overshoot (or undershoot) can be avoided if the interface values were to remain between the adjacent cell averaged values. We can limit the slope computed by the LS method to satisfy this criterion. For a one dimensional case, the interface value computed from the left cell i is

$$u_{i+\frac{1}{2}}^{left} = u_i + C_i(x_{i+\frac{1}{2}} - x_i) \quad (15)$$

where C_i is $\partial u / \partial x$. Consider the case $u_i \leq u_{i+1}$. Referring to Fig. 14, the reconstructed value $u_{i+\frac{1}{2}}^{left}$ is required to lie within the adjacent cell averaged values

$$u_i \leq u_{i+\frac{1}{2}}^{left} \leq u_{i+1} \quad (16)$$

or

$$0 \leq C_i \leq \frac{u_{i+1} - u_i}{x_{i+\frac{1}{2}} - x_i} \quad (17)$$

This is achieved by replacing the gradient C_i by ηC_i where

$$\eta = \begin{cases} 1 & \text{for } 0 \leq C_i \leq \frac{u_{i+1} - u_i}{x_{i+\frac{1}{2}} - x_i} \\ \frac{1}{C_i} \frac{u_{i+1} - u_i}{x_{i+\frac{1}{2}} - x_i} & \text{for } C_i > \frac{u_{i+1} - u_i}{x_{i+\frac{1}{2}} - x_i} \\ 0 & \text{for } C_i < 0 \end{cases} \quad (18)$$

An analogous result can be obtained for the case $u_i > u_{i+\frac{1}{2}}$.

For a general 3D configuration, the limited quantities are

$$u_{i,j}^{left} = u_i + \eta \vec{C} \cdot \vec{\Delta x} \quad (19)$$

where $u_{i,j}^{left}$ is the reconstructed value of variable u for cell i and the face adjacent to cell j , and

$$\vec{C} \cdot \vec{\Delta x} = \begin{pmatrix} Cx_i \\ Cy_i \\ Cz_i \end{pmatrix} \cdot \begin{pmatrix} x_{i,j} - x_i \\ y_{i,j} - y_i \\ z_{i,j} - z_i \end{pmatrix} \quad (20)$$

affecting the undisturbed boundary layer.

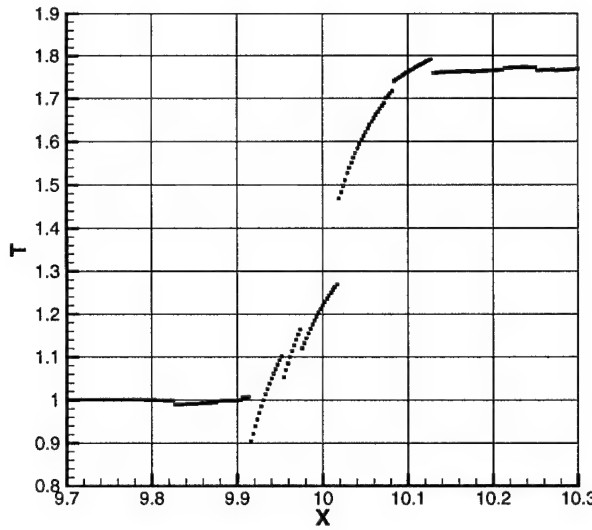


Figure 15: Temperature (no limiter)

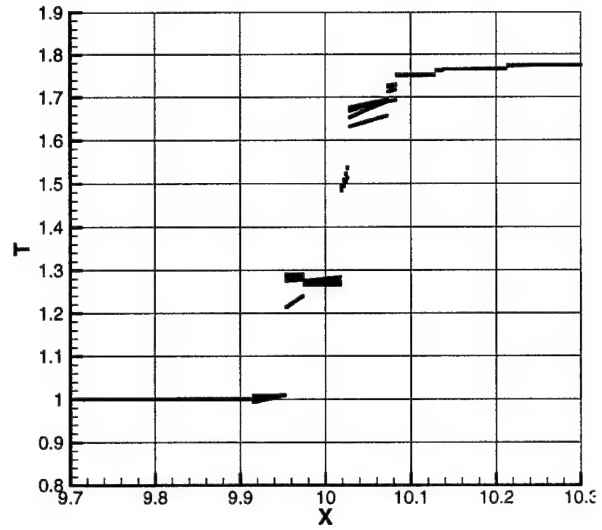


Figure 16: Temperature (homogeneous limiter)

$$\eta = \begin{cases} 1.0 & \text{for } 0 \leq \vec{C} \cdot \vec{\Delta x} \leq u_j - u_i \\ \frac{u_j - u_i}{\vec{C} \cdot \vec{\Delta x}} & \text{for } \vec{C} \cdot \vec{\Delta x} > u_j - u_i \\ 0 & \text{for } \vec{C} \cdot \vec{\Delta x} < 0 \end{cases} \quad (21)$$

The above expression holds for $u_i \leq u_j$. An analogous expression holds for $u_i > u_j$. In practice the limiter is successively applied to the different cell neighbors j of the cell i . As far as tetrahedras are concerned, only the neighbors sharing a face are used.

A 25° compression corner computation has been designed to evaluate the efficiency of the limiter. Fig. 15 displays the evolution of the static temperature across the shock computed using the second order LS without a limiter. Strong overshoots and undershoots appear. Fig. 16 displays the static temperature in the shock using this limiter. The spurious oscillations disappear, although the gradients within the cells appear to have been reduced probably more than necessary.

2.4 Inhomogeneous Limiter

The homogeneous limiter (21) does not treat the function gradients Cx_i, Cy_i, Cz_i independently, and therefore is overly limiting. Consider a case where Cx_i and Cy_i are “satisfactorily” computed but Cz_i is overestimated by the LS method and therefore $u_{i,j}^{left}$ is also overestimated. During the limitation process η is set to a value less than 1 because $\vec{C} \cdot \vec{\Delta x}$ is too large. As a result, all three gradients are reduced, even though Cx, Cy were “satisfactory”.

A three parameter limiter is defined by

$$u_{i,j}^{left} = u_i + \begin{pmatrix} \eta_x Cx_i \\ \eta_y Cy_i \\ \eta_z Cz_i \end{pmatrix} \cdot \begin{pmatrix} x_{i,j} - x_i \\ y_{i,j} - y_i \\ z_{i,j} - z_i \end{pmatrix} \quad (22)$$

wherein each gradient Cx_i, Cy_i, Cz_i has a limiter. We present the inhomogeneous limiter for $u_i \leq u_j$. Analogous expressions hold for $u_i > u_j$.

Case 1: $\vec{C} \cdot \vec{\Delta x} > u_j - u_i$

$$\begin{aligned}\eta_x &= 1.0 - k_1 \left| \frac{Cx_i(x_{i,j} - x_i)}{k_2} \right| \\ \eta_y &= 1.0 - k_1 \left| \frac{Cy_i(y_{i,j} - y_i)}{k_2} \right| \\ \eta_z &= 1.0 - k_1 \left| \frac{Cz_i(z_{i,j} - z_i)}{k_2} \right|\end{aligned}\tag{23}$$

where

$$k_1 = \frac{\hat{u}_{i,j}^{left} - u_j}{\hat{u}_{i,j}^{left} - u_i}\tag{24}$$

$$k_2 = \max \left\{ \begin{array}{l} Cx_i \cdot (x_{i,j} - x_i) \\ Cy_i \cdot (y_{i,j} - y_i) \\ Cz_i \cdot (z_{i,j} - z_i) \end{array} \right\}\tag{25}$$

where \hat{u}^{left} is the reconstructed value assuming $\eta_x = \eta_y = \eta_z = 1$.

Case 2: $0 \leq \vec{C} \cdot \vec{\Delta x} \leq u_j - u_i$

$$\eta_x = 1\tag{26}$$

$$\eta_y = 1\tag{27}$$

$$\eta_z = 1\tag{28}$$

Case 3: $\vec{C} \cdot \vec{\Delta x} < 0$

$$\eta_x = 0\tag{29}$$

$$\eta_y = 0\tag{30}$$

$$\eta_z = 0\tag{31}$$

The process mainly limits the components η_x, η_y, η_z whose contribution in the $\vec{C} \cdot \vec{\Delta x}$ expression is the largest. When the j neighbor position is aligned with x, y or z direction, then only Cx, Cy or Cz is respectively reduced.

Fig. 17 displays the results of this limiter for the static temperature profile within the shock. The effect on the gradient is less severe than in Fig. 16. The 25° compression corner computations described below use this limiter.

2.5 ENO scheme

The key idea of ENO schemes is to use the smoothest stencil among several candidates to approximate the fluxes at cell boundaries to a high order accuracy and at the same time to avoid spurious oscillations near shocks. We previously computed supersonic turbulent flow past compression corner of 8° at Mach 3 without use of limiters (Urbain 1999). However, the 25° compression corner at Mach 3 (see Fig. 18) requires a limiter, and thus determination of the most effective limiter is the objective of this part of our study. In the 25° compression corner, a strong shock is formed through a series of unsteady compression waves, and variations in the flow variables in the boundary layer are sometimes comparable to the shock. In order to determine a proper criterion to construct the ENO stencil, we begin with the analysis of the variable gradient (we use density since it has a similar change as the other variables), shown in Fig. 19 at $x = 3\delta$, where x is measured from the corner and δ is the inflow boundary layer thickness. The density is non-dimensionalized by the

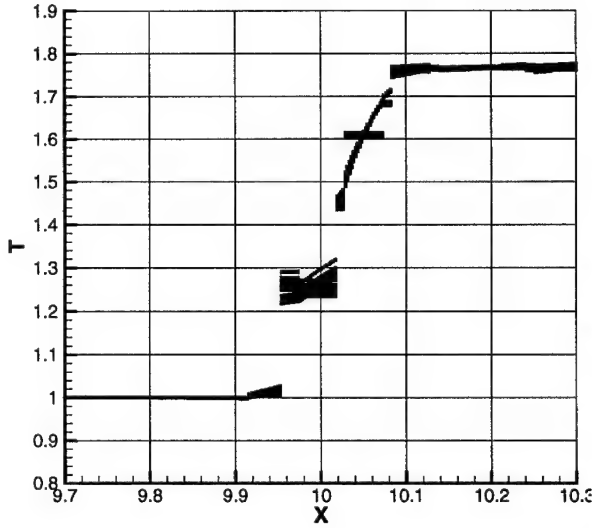


Figure 17: Temperature (inhomogeneous limiter)

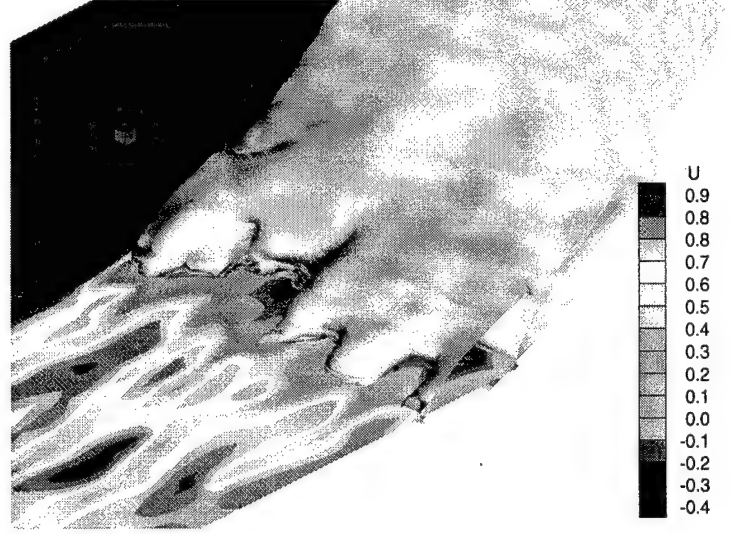


Figure 18: 25° compression corner

freestream density ρ_∞ . The gradient using the isotropic stencil (Okongo 1998) with Least Squares reconstruction shows two peaks corresponding to the boundary layer and the shock wave. Outside these two regions, the change of the gradient is smooth. The selection of the ENO stencil should take advantage of this feature and make the ENO stencil focus on these two regions.

First, we establish a criterion to decide where to use the ENO stencil. The density ratio across the shock is approximately 2.19 according to the Rankine-Hugoniot equations. The maximum norm of the density gradient α is approximately equal to 6 with mesh spacing $\Delta r = \sqrt{\Delta x^2 + \Delta y^2 + \Delta z^2} = 0.2$ in the vicinity of the shock, where Δr is non-dimensionalized by δ . We make a cut-off at $\alpha = 6$ and any cell whose density gradient is larger than α should use an ENO stencil. We define Σ as a set of cells satisfying $|\nabla \rho| > \alpha$. In Fig. 19, the maximum density gradient based on the isotropic stencil is approximately 13.

Second, for all Σ , a direction should be found to construct the ENO stencil. Consider any tetrahedron in Σ in which four possible density gradients are computed using only three face neighbors, denoted as $|\nabla \rho|_k$ ($k = 0, 1, 2, 3$). The subscript is the index of the face neighbor which has been excluded. The density gradients are computed by the Least Squares method. We assume that

$$|\nabla \rho|_3 \geq |\nabla \rho|_2 \geq |\nabla \rho|_1 \geq |\nabla \rho|_0$$

where $|\nabla \rho|_{\max} = |\nabla \rho|_3$, $|\nabla \rho|_{\min} = |\nabla \rho|_0$.

We construct the ENO stencil as follows. First, the three face neighbors which give the minimum density gradient are added. Second, we find all the node neighbors of any cell of Σ and exclude all the cells which share at least one node with the remaining face neighbor. Any five of the remaining cells which are the node neighbors of that cell and these three face neighbors are used to construct the ENO stencil.

A modified Riemann shock tube case with the initial pressure ratio of ten and an initial distribution of isotropic turbulence is used to verify the ENO scheme and to compare with the inhomogeneous limiter. The pressure ratio across the shock is chosen close to that in the 25° compression corner. The cut-off number α is set to 6. Fig. 20 shows the comparison between the inhomogeneous limiter and the ENO scheme for the Riemann shock tube case. It can be seen that the ENO stencil is

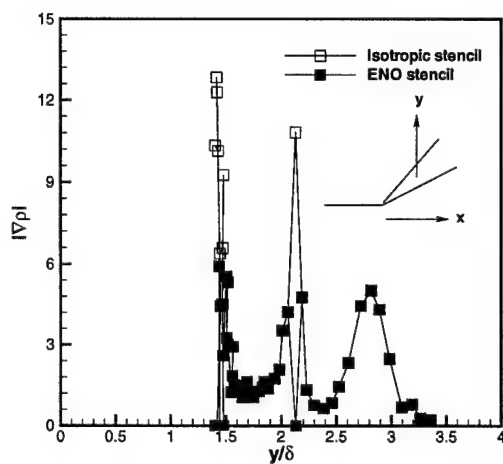


Figure 19: $|\nabla\rho|$ vs y/δ

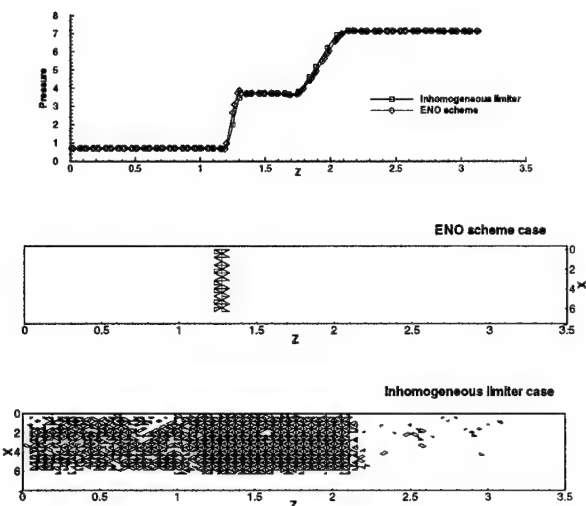


Figure 20: ENO cells for a Riemann shock tube

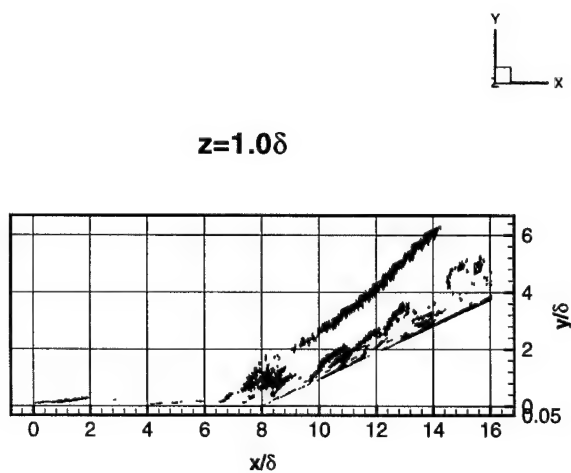


Figure 21: ENO cells for 25° compression corner

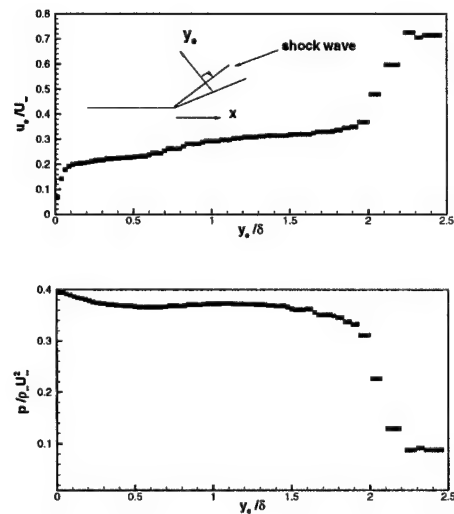


Figure 22: Flowfield behaviour across shock

used only in the shock region, while the inhomogeneous limiter is also used in the expansion fan region where there are no overshoots and even in the undisturbed flow in presence of turbulence. In Fig. 21, the ENO scheme is applied to the 25° compression corner with $\alpha = 6$. The cells using the ENO stencil appear principally in the shock region and the boundary layer downstream of the corner where the density gradient has a larger variation than the upstream. Fig. 22 shows the instantaneous profiles of velocity and pressure along the direction perpendicular to the shock wave at $z = 1.0\delta$ (where y_e is measured along the direction perpendicular to the shock wave and U_∞ is the streamwise velocity in the freestream.). The x coordinate of the interception point of the y_e with the solid wall is 5δ , where x is measured from the corner. The shock wave is efficiently limited within the width of two or three cells.

2.6 Results

David (1993) performed the first LES of a compression corner which successfully reproduced the Taylor-Görtler vortices downstream of the shock. Nevertheless, the use of a pseudo-compressible subgrid-model did not permit accurate quantitative results. The second and most recent LES was Hunt and Nixon (1995) who investigated the role played by turbulence, and showed a direct correlation between the shock motion and the incoming velocity fluctuations. They also demonstrated that the size of the separation bubble has, to some extent, a weak effect on the shock motion. Despite the lack of detail in the inner layer (a log-law wall function was used on a rough grid resolution), it displayed the qualitative features of the shock oscillation observed experimentally (Dolling and Or 1983).

A computation of an adiabatic turbulent boundary layer flow past a 25° compression corner at Mach 3.0 and $Re_\delta = 2 \times 10^4$ was performed.

Allowing x, y and z to denote the streamwise, transverse and spanwise directions, respectively, the computational domain is $L_x = 16.0\delta$, $L_y = 3.4\delta$, and $L_z = 1.925\delta$. The grid consists of $213 \times 35 \times 57$ nodes in the x, y and z directions, respectively. The reference quantities for non-dimensionalization are length δ (the incoming boundary layer thickness), velocity U_∞ , density ρ_∞ , static temperature T_∞ and molecular viscosity μ_∞ (where the subscript ∞ denotes the freestream conditions upstream of the compression corner). The tetrahedral grid is employed and stretched in the y direction with a spacing of 0.008δ at the wall and the stretching factor of 1.154. The grid is concentrated around the compression corner. The details of the grid are shown in Table 6, wherein $\Delta y^+ = \Delta y/\eta$ with

Table 6: Details of Grids								
Name	Mach	Δx^+	Δy^+ at the wall	Δz^+	$\Delta x/\delta$	$\Delta y/\delta$ at $y = \delta$	$\Delta z/\delta$	Tetras
Theoretical value	2.88	24	1.9	8.1	0.1	0.14	0.034	
LES	2.88	20.9	1.67	7.1	0.1	0.14	0.034	2,018,240

the inner length scale $\eta = \nu_w/u_\tau$ (ν_w is the kinematic viscosity at the wall, $u_\tau = \sqrt{\tau_w/\rho_w}$ is the friction velocity, τ_w is the wall shear stress and ρ_w is the density at the wall). The theoretical values of u_τ and ν_w are obtained from the combined Law of the Wall and Wake evaluated at $y = \delta$ and the power law of the relationship between temperature and kinematic viscosity, respectively.

The inflow condition is obtained from a separate flat plate boundary layer computation. The non-

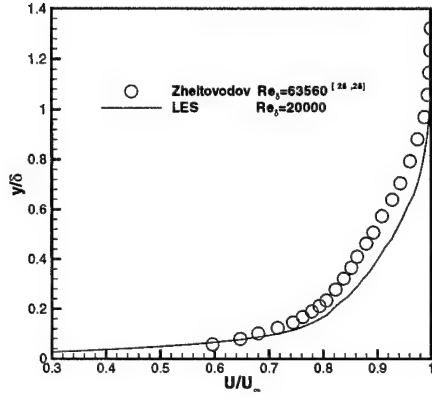


Figure 23: Mean streamwise velocity

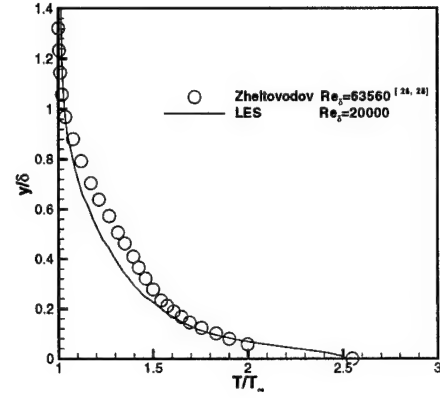


Figure 24: Mean temperature

slip boundary condition is used to the adiabatic wall. All the flow variables shown in the figures are averaged in time and the spanwise direction. The time averaging period is set to three times the flow-through time, where one flow-through time is defined as the time for the freestream flow to traverse the computational domain. The details are presented in Urbin *et al* 1999.

The oncoming flow characteristics are illustrated by the mean flow variables in Fig. 23 and Fig. 24 and the Reynolds shear stress in Fig. 25. The comparisons with experiments (Zheltovodov *et al* 1990) and DNS show good agreement.

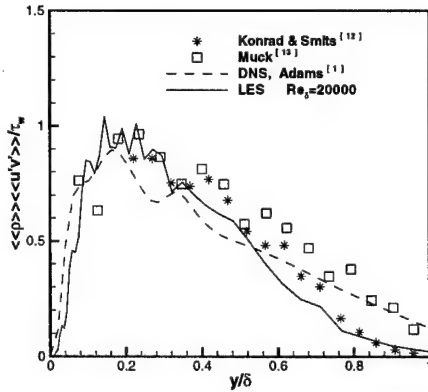


Figure 25: Reynolds shear stress

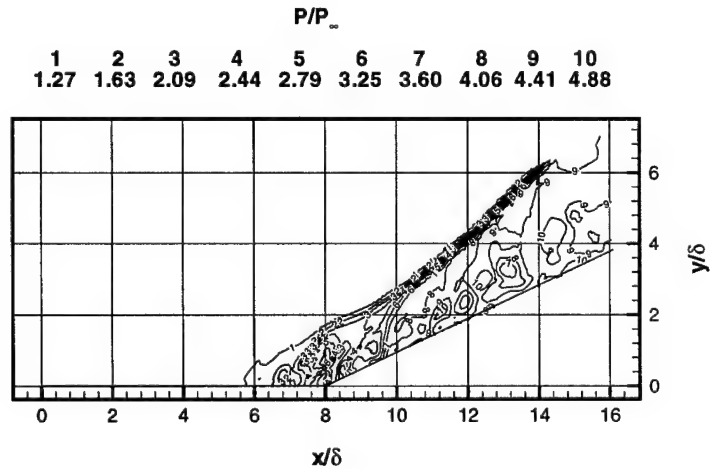


Figure 26: Instantaneous pressure contour

Fig. 26 shows the pressure contour distribution at $x - y$ plane of $z = 1.0\delta$. A strong separation and attachment shock wave is formed at the compression corner leading to the higher pressure level

after the shock. The strong adverse pressure gradient causes the skin friction coefficient to decrease dramatically and the flow separates. Downstream of the corner, the overall increase in pressure and the decrease in Mach number cause the skin friction coefficient to recover.

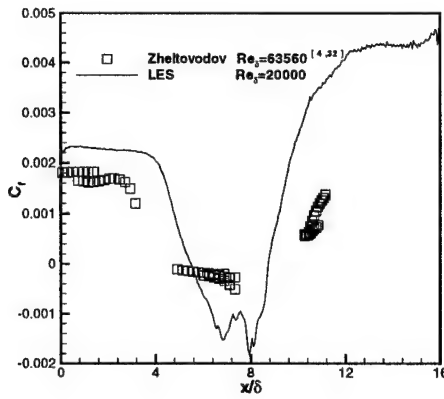


Figure 27: Skin friction coefficient

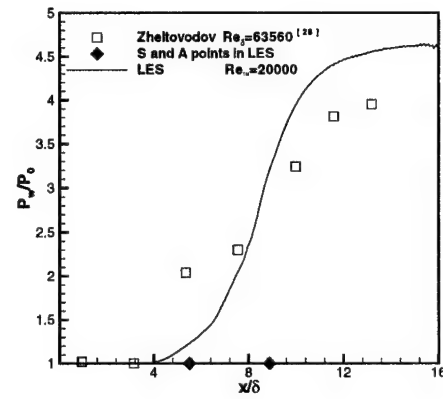


Figure 28: Surface wall pressure

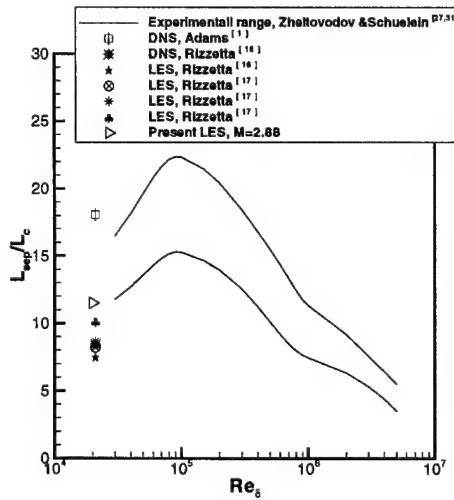


Figure 29: Separation length for LES and DNS

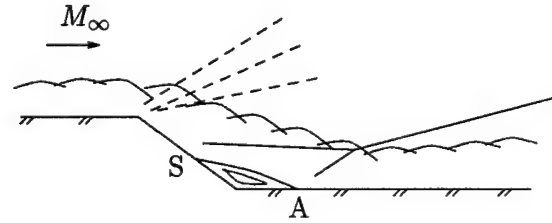


Figure 30: Expansion-compression corner

The computational results are shown in Fig. 27–Fig. 29 along with experimental data. The skin friction coefficient in Fig. 27 is compared with the experiment at higher Reynolds number of $Re_\delta = 63560$. According to the Law of the Wall and Wake, the friction velocity is decreased with the increase in Reynolds number, leading to the higher skin friction coefficient in the computation. The time and spanwise averaged surface pressure profile along the streamwise direction is compared with experiment at higher Reynolds number in Fig. 28 and the pressure plateau is not observed. The difference between the predicted and experimental surface pressure profile may be attributable to the difference in Reynolds number.

The effect of Reynolds number on the separation length is plotted in Fig. 29. In this figure, the separation length is measured by connecting the separation and attachment points at which the

time and spanwise averaged skin friction coefficients go to zero and then scaled by the characteristic length (L_c) proposed by Zheltovodov and Schuelein 1987, 1993.

$$L_c = \delta(p_2/p_{pl})^{3.1}/M_\infty^3 \quad (32)$$

where δ is the incoming boundary layer thickness, p_2 is the pressure after the shock in inviscid flow, p_{pl} is the plateau pressure obtained by the empirical formula $p_{pl} = p_\infty(0.5M_\infty + 1)$ (Zukoski 1967) and M_∞ is the Mach number in the uniform flow. Some LES and DNS results by other researchers are also plotted in Fig. 29 for comparison. Our LES successfully predicts the consistent trend with the experiment.

3 Expansion-Compression Corner

Supersonic expansion-compression corner (Fig. 30) is reminiscent of aerodynamic configurations wherein a supersonic boundary layer is subjected to an initial expansion followed by a subsequent compression. Interest in this configuration is due in part to the stabilizing influence of the expansion (Dussauge 1987, Zheltovodov *et al* 1987, Zheltovodov and Schuelein 1987, Smith 1997, Stephen 1998, Zheltovodov 1990). The first systematic combined experimental and numerical study of an expansion-compression corner by Zheltovodov 1992 and Zheltovodov 1993 showed that several different turbulence models (including $k-\epsilon$, $q-\omega$ and several modifications thereto) did not accurately predict the separation and attachment positions, and distributions of surface skin friction and heat transfer. We therefore seek to ascertain the capability of LES to predict this flowfield.

An incoming Mach 3 adiabatic equilibrium turbulent boundary layer of height δ expands over a 25° corner followed by a 25° compression. The distance along the expansion surface is 7.1δ (*i.e.*, the vertical distance between the two horizontal surfaces is 3δ , and the horizontal distance between the expansion and compression corners is 6.43δ).

The Cartesian coordinates x, y and z are aligned in the incoming streamwise, transverse and spanwise directions with the origin at the inflow boundary. The computational domain is $L_x = 24.0\delta$, $L_y = 3.4\delta$, and $L_z = 1.925\delta$. The expansion corner is located at 4δ from the inflow boundary. The grid consists of $253 \times 35 \times 57$ nodes in the x, y and z directions, respectively, forming 479,808 hexahedra which are subdivided into five tetrahedra each. Thus, the total number of tetrahedra is 2,399,040. The grid is stretched in the y direction with spacing 0.008δ at the wall and a geometric stretching factor of 1.154. The grid is concentrated in the streamwise direction in the neighborhood of the expansion and compression corners. The details are shown in Table 7 where $\Delta y^+ = \Delta y u_\tau / \nu_w$ where ν_w is the computed kinematic viscosity at the wall, $u_\tau = \sqrt{\tau_w / \rho_w}$ is the friction velocity, τ_w is the computed wall shear stress and ρ_w is the computed density at the wall. The grid is consistent with the resolution requirements for the LES code established by Urbin 2001.

Table 7: Details of Grid							
Name	Δx^+	Δy^+	Δz^+	$\Delta x/\delta$	$\Delta y/\delta$	$\Delta z/\delta$	Tetras
		at the wall			at $y = \delta$		
Computed	20.9	1.67	7.1	0.1	0.14	0.034	2,399,040

The inflow boundary condition is obtained from a separate flat plate boundary layer computation. Experimental data has been obtained by Zheltovodov *et al* 1987, Zheltovodov and Schuelein 1987, Zheltovodov 1990a and presented in part in tabular form in Zheltovodov 1990 for the expansion-

compression corner at Mach 3 and several Reynolds numbers Re_δ based on the incoming boundary layer thickness δ . The experimental conditions are listed in Table 8, where FPBL and ECC imply flat plate boundary layer and expansion-compression corner, respectively. The LES was performed at a lower Reynolds number ($Re_\delta = 2 \times 10^4$) than the experiment ($Re_\delta = 4.4 \times 10^4$ to 1.94×10^5) for reasons of computational cost. Additional LES cases will be performed at higher Reynolds numbers.

Table 8: Details of Experiments and Computation

Cases	Mach	Re_δ	References
ECC	2.9	4.07×10^4	Zheltonovodov 1990
ECC	2.9	6.76×10^4	Zheltonovodov 1990
ECC	2.9	8.0×10^4	Zheltonovodov 1990
ECC	2.9	1.94×10^5	Zheltonovodov1987 and Zheltonovodov 1990a
ECC	2.88	2.0×10^4	Present computation
FPBL	2.88	1.33×10^5	Zheltonovodov 1990a

The structure of the flowfield is shown in Figs. 31 and Fig. 32 which display the mean static pressure and streamlines at $z = \delta$. The flow expands around the first corner, and recompresses at the second corner through a shock which separates the boundary layer as evident in Fig. 32. The flowfield structure is in good agreement with the results of Zheltonovodov 1987, Zheltonovodov 1988, Zheltonovodov 1990 and Zheltonovodov 1990a which are shown qualitatively in Fig. 30.

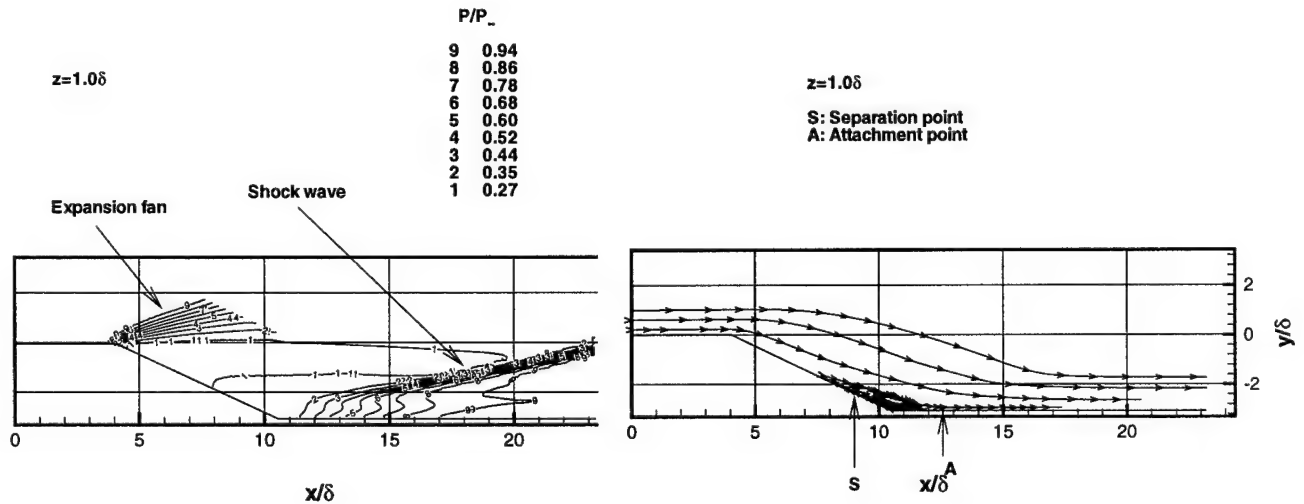


Figure 31: Mean static pressure (s is separation, Figure 32: Mean streamlines (s is separation, A is attachment)

The mean velocity profiles in the x -direction are shown in Fig. 33 at $x = 2\delta$ and $x = 6\delta$, where x is measured from the inflow along the direction of the inflow freestream velocity (Fig. 31). The abscissa is the component of velocity locally parallel to the wall, and the ordinate is the distance measured normal to the wall. The first profile is upstream of the expansion corner which is located at $x = 4\delta$, and the second is downstream of the expansion fan and upstream of the separation point. The computed mean velocity profile at the first location is slightly fuller than the experiment. This is consistent with the experimentally observed dependence of the exponent n in the power-law $U/U_\infty = (y/\delta)^{1/n}$ on the Reynolds number. The second profile shows a significant acceleration of

the flow in the outer portion of the boundary layer due to the expansion.

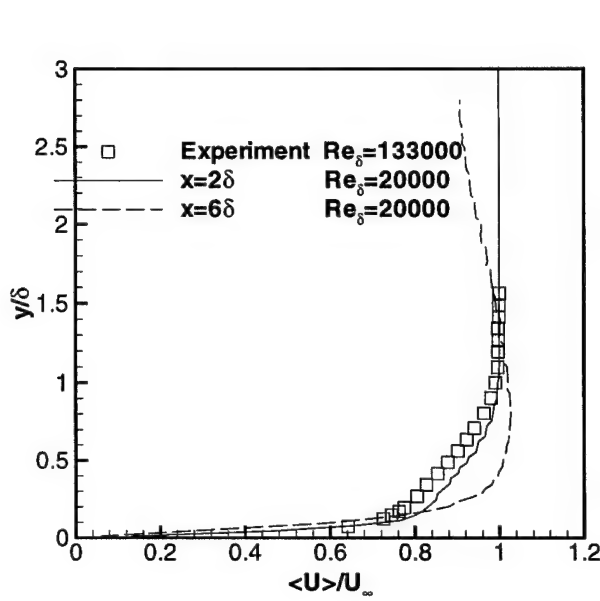


Figure 33: Mean velocity

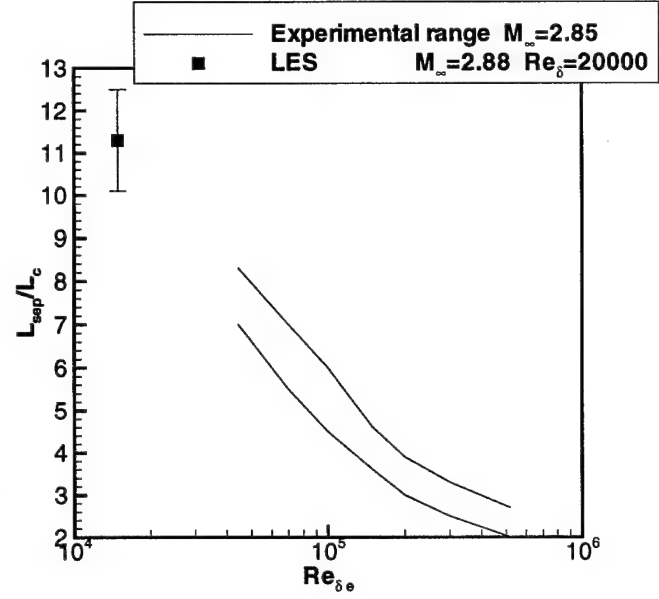


Figure 34: Separation length

Zhel'tovodov 1988 and Zhel'tovodov 1993 developed an empirical correlation for the separation length (defined as the minimum distance between the mean separation and attachment points on the wall) in the expansion-compression corner interaction. The scaled separation length L_{sep}/L_c is observed experimentally to be a function of Re_{δ} where the characteristic length (L_c) is defined by

$$L_c = \delta_e (p_2/p_{pl})^{3.1} / M_e^3 \quad (33)$$

where δ_e is the incoming boundary layer thickness (upstream of the expansion corner), p_2 is the pressure after the shock in inviscid flow, p_{pl} is the plateau pressure from the empirical formula $p_{pl} = p_e (\frac{1}{2} M_e + 1)$ where p_e and M_e are the static pressure and freestream Mach number upstream of the compression corner and downstream of the expansion fan. In the computation, the location is taken to be $x = 6\delta$. The values of M_e and p_2 have been computed using inviscid theory. Also, $Re_{\delta_e} = 1.8 \times 10^4$ for LES ($Re_{\delta_e} = \rho_e U_e \delta_e / \mu_e$, where ρ_e , U_e and μ_e are computed using inviscid theory). The experimental data correlation of Zhel'tovodov 1988 and the computed result² for the scaled separation length is shown in Fig. 34. The computed value is consistent with a linear extrapolation of the experimental data.

The surface pressure profile in Fig. 36 displays a pressure plateau on the compression face generated by the separation bubble. The experiments exhibit a trend of increase in the size of the pressure plateau region with decreasing Reynolds number. The experimental data at the lowest Reynolds number ($Re_{\delta} = 4.1 \times 10^4$) shows close agreement with the computed results for $Re_{\delta} = 2 \times 10^4$ for the location, extent and magnitude of the pressure plateau. Moreover, the shape of the experimental pressure plateau shows little variation for $Re_{\delta} \leq 6.8 \times 10^4$, thus suggesting that the computed pressure plateau region (for $Re_{\delta} = 2 \times 10^4$) is accurate. The computed recovery of the surface pressure is more rapid than in the experiment, however.

²The uncertainty in the computed value of L_{sep}/L_c is associated with the uncertainty in determining δ_e . We have used the streamwise Reynolds stress ($\langle \rho \rangle \langle u'u' \rangle$) to determine δ_e (Fig. 35), where u' is the fluctuating velocity parallel to the wall.

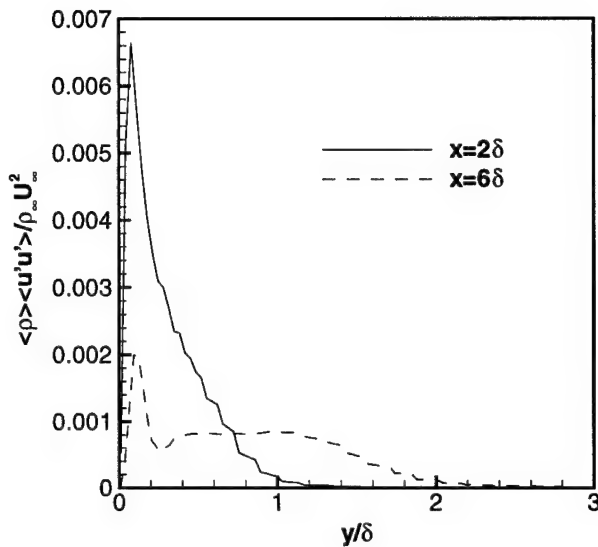


Figure 35: Reynolds streamwise stress

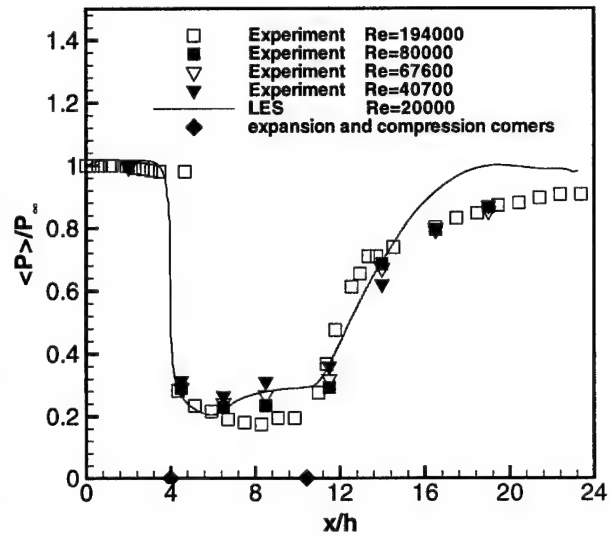


Figure 36: Surface pressure

The computed and experimental mean skin friction coefficient $c_f = \tau_w / \frac{1}{2} \rho_\infty U_\infty^2$ are shown in Fig. 37. The computed separation and attachment points are evident. The skin friction rises rapidly downstream of attachment. The computed results at $Re_\delta = 2 \times 10^4$ are in close agreement with the experimental data at $Re_\delta = 8.0 \times 10^4$ and 1.94×10^5 in the region downstream of reattachment.

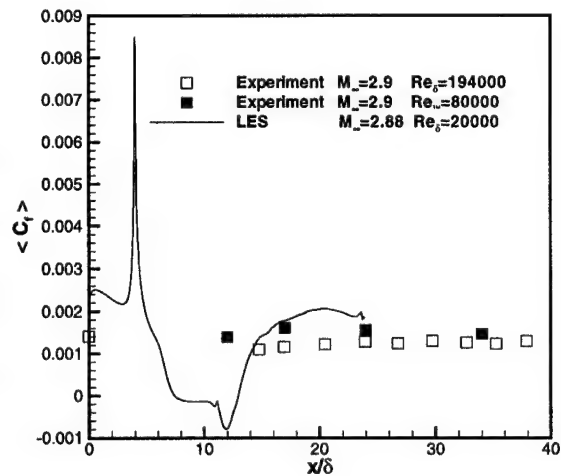


Figure 37: Skin friction coefficient

4 ^{Subsonic} Square Jet

Turbulent round and plane jets are simple inhomogeneous flows that can be served to verify models for complex flows and have been experimentally and numerically studied extensively (Panchapakesan 1993, Rodi 1980). Recently, noncircular jets have been gained much interest in passive control due to their enhanced jet mixing properties (Grinstein 1992, Grinstein 1995a, Grinstein 1995b, Grinstein 2001, Gutmark 1999). A square jet at a Reynolds number of 3200 and a Mach number of 0.3 is simulated. Temporal evolutions are visualized to characterize the dynamics of deforming vortex rings, ribs and their interactions. Statistical quantities are quantified and compared with the DNS results of Grinstein et al 1995.

The grid consists of $65 \times 65 \times 65$ hexahedral cells in an unstructured grid covering a computational domain of $5D$ in the streamwise direction and $\pm 3D$ along the transverse directions. Each hexahedral cell is divided into five tetrahedral cells, yielding a total of 1.3M tetrahedra. A uniform grid is used along the streamwise direction with the hexahedral grid spacing of $\Delta x/D = 0.078$, which is larger than 0.04 used by Grinstein et al. in their DNS (Grinstein 1995). The grids are stretched along the other two directions and the minimum grid spacings are $\Delta y/D = \Delta z/D = 0.0375$. The imposed boundary conditions include inflow, outflow and wall boundaries. At the inflow, the streamwise velocities are prescribed as

$$u = U[1 + A \sin(2\pi ft)] \quad (34)$$

and

$$U = 0.5 U_\infty [1 - \tanh[b_2(2|y|/D - D/(2|y|))] \times 0.5 U_\infty [1 - \tanh[b_2(2|z|/D - D/(2|z|))], \quad (35)$$

where $A = 0.02$ is the perturbation amplitude, f is the forcing frequency ($f = 0.5$), $b_2 = 0.25R_{1/2}/\theta$, where $R_{1/2}/\theta = 40$, $R = D/2$ and θ is the momentum thickness. Zero-gradient condition is imposed at the outlet and symmetry boundary conditions are used at the side walls.

The iso-surfaces of the total vorticity $\omega = \sqrt{\omega_x^2 + \omega_y^2 + \omega_z^2}$ corresponding to $\omega = 0.25\omega_{peak}$ are shown in Fig. 38. Azimuthal nonuniformities make the evolution of the jet shear layer more complicated relative to circular jets. Close to the jet exit, a smooth square vortex sheet can be observed, and subsequently rolled-up vortex-ring structures form due to shear-layer Kelvin-Helmholtz instability. However, the vortex rings further downstream deform to non-planar shape due to self-induction mechanism caused by azimuthal nonuniformities. The deformed vortex rings are connected with the four corners of the initial square sheet by ribs. The hairpin braid vortices aligned with the corners progress faster in the diagonal direction than the others, "which results in redistribution of energy between azimuthal and streamwise vortices" (Grinstein 2001). Further downstream, the jet development is characterized by the strong interaction between vortex rings and braid vortices, which leads to a final breakdown of the large-scales coherent structures and transition to the turbulent flow. The self-induced deformation of the rings and rib pair were explained to be the leading mechanism for larger entrainment properties in non-circular jets relative to circular jets (Grinstein 1992). "The interactions between the streamwise vortices and the vortex rings is reminiscent of the interaction between ribs and spanwise rollers in the mixing layer" (Grinstein 1992). Mixing of jets with surroundings can be enhanced through controlling the formation, development and interaction of large-scale coherent structures passively.

Fig. 39 shows the instantaneous crosswise vorticity $\omega_z = \partial v/\partial x - \partial u/\partial y$ contours at the central $x - y$ plane. Rolled-up structures can be observed near the base, and subsequently symmetrical

counterrotating toroidal structures form in the shear layer which are then followed by their stretching and deformation. The organized structures can be broken down into smaller eddies further downstream. Evidently, the MILES model can capture the transition process. Large-scale vortex rings dominate in the near-field and the small vortices dominate downstream after the breakdown. The spatial spreading can be clearly observed downstream as the jet spreads by entraining mass from the surrounding nonvortical fluid.

Fig. 40 (a-d) shows the contours of instantaneous streamwise vorticity, $\omega_x = \partial v / \partial z - \partial w / \partial y$, across the $y - z$ planes of $x/D = 1, 2, 3$ and 4. Quite different behaviour can be observed at different axial positions. Vortex shears with some rounded-corners are stretched and thickened but still keep the initial square shape at the position of $x/D = 1$. The jet cross section switches axis 45° relative to that of the jet nozzle at the axial location of $x/D = 2, 3$ due to self-induced velocity around the corners by the presence of streamwise vorticity. The flow structure develops into a irregular shape further downstream at $x/D = 4$.

The statistical quantities are obtained by averaging over five forcing cycles after a statistically stationary state has been reached after an elapsed dimensionless physical time of ten. The centerline distributions of the mean axial velocity by LES compared with the DNS results of Grinstein *et al* 1995 are plotted in Fig. 41. The mean velocity initially decays within the first 1.5 diameters and subsequently shows a slight increase due to the periodic roll-up by the sinusoidal forcing. The decay after 3.2 diameters is the result of turbulent mixing. In general, the agreement between present MILES and previous DNS results are good.

The corresponding centerline r.m.s. velocities u'/U_c are shown in Fig. 42. Note that close to the inflow plane the r.m.s. of velocity fluctuations is about 2 percent and corresponds to the imposed disturbance level. In the potential core region, the r.m.s. velocity decreases slightly with increasing axial distance which shows a tendency to remain laminar with low turbulence intensities. Beyond the end of the potential core, the fluctuations of velocity increase very rapidly, which indicates the appearance of the secondary-instability mechanism which leads to the final breakdown of the large vortex structures. Due to insufficient length scale in the streamwise direction, the self-similar behaviour has not been achieved. However, it can be seen that the agreement between MILES and DNS is very good for the transient square jet.



Figure 38: Instantaneous isosurfaces of total vorticity $\omega = 0.25\omega_{peak}$.

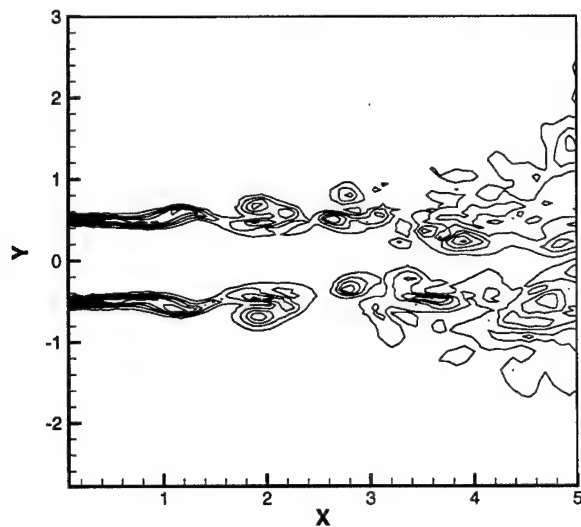
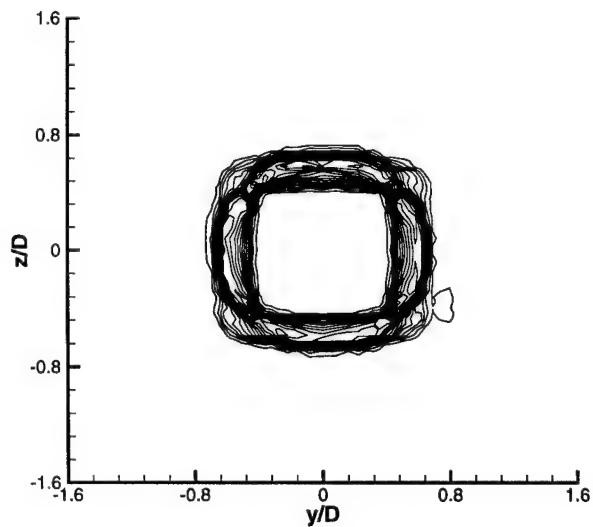
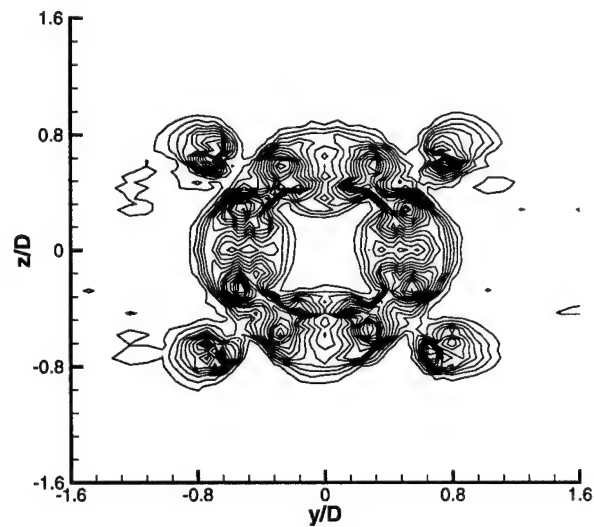


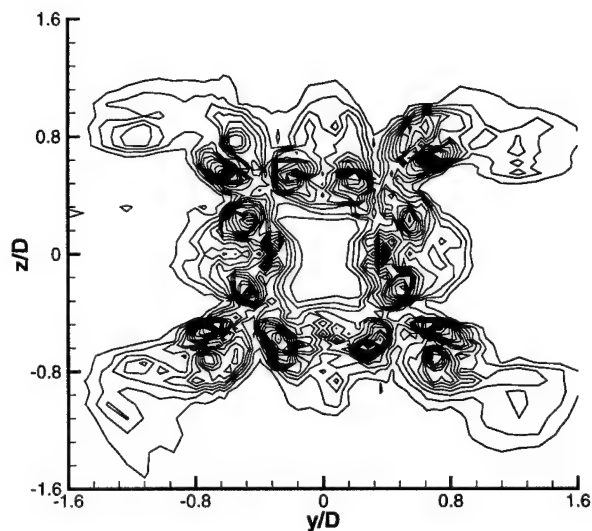
Figure 39: Instantaneous streamwise vorticity contours at the $x - y$ centre-plane.



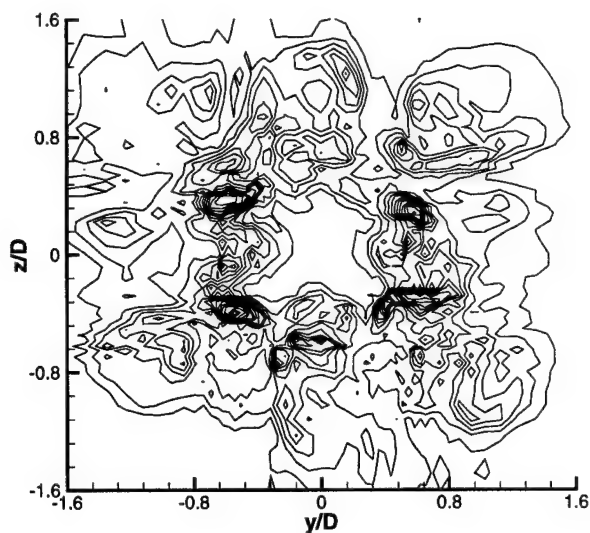
(a)



(b)



(c)



(d)

Figure 40: Instantaneous streamwise vorticity contours across the $y - z$ planes at $x/D =$ (a) 1, (b) 2, (c) 3 and (d) 4.

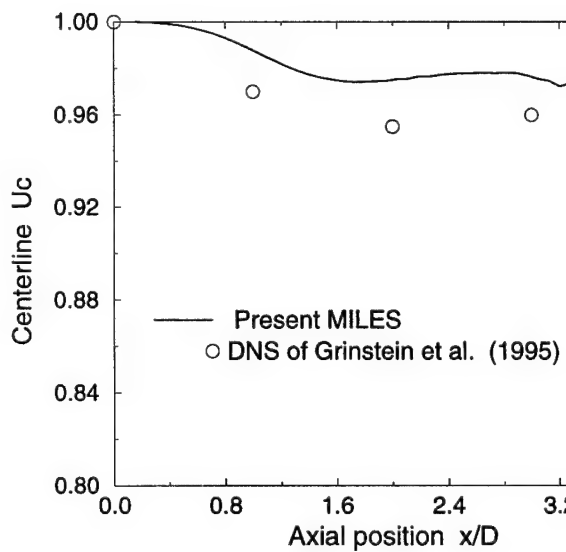


Figure 41: Centerline profiles of the mean velocity.

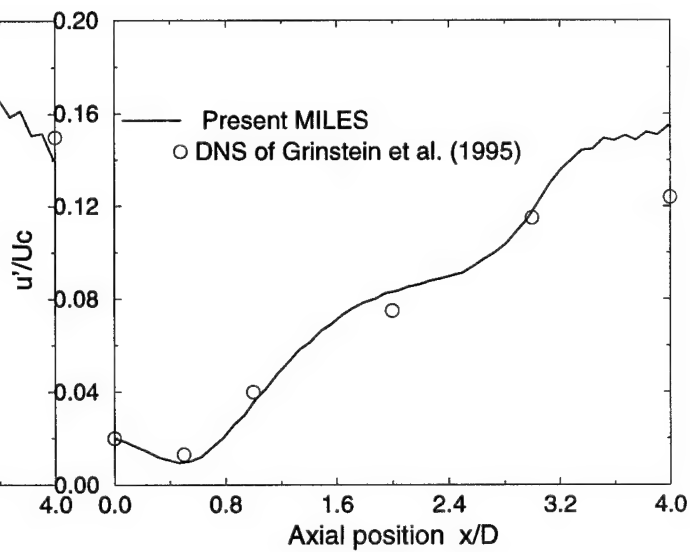


Figure 42: Centerline profiles of the r.m.s. axial velocity.

Personnel

The personnel of the research project are listed in Table 9.

Table 9: Personnel

Name	Title	Period of Participation	Supported by
Prof. Doyle Knight	Principal Investigator	Dec 98 - Mar 02	this grant and Rutgers
Dr. Frederic Thivet	Visiting Scientist	Dec 98 - Aug 00	ONERA
Dr. Gerald Urbin	Postdoctoral Associate	Dec 99 - Nov 99	this grant
Dr. Hong Yan	Research Associate	Sept 99 - Mar 02	this grant
Dr. Xu Zhou	Postdoctoral Associate	Nov 00 - Aug 01	this grant

Journal Publications

Zheltovodov, A., Maksimov, A., Shevchenko, A., and Knight, D., "Topology of Three-Dimensional Separation under the Conditions of Asymmetrical Interaction of Crossing Shocks and Expansion Waves with Turbulent Boundary Layer", *Thermophysics and Aeromechanics*, Vol. 5, No. 4, 1998, pp. 483-503.

Okong'o, N., Knight, D., and Zhou, G., "Large Eddy Simulations Using an Unstructured Grid Compressible Navier-Stokes Algorithm", *International Journal of Computational Fluid Dynamics*, Vol. 13, 2000, pp. 303-326.

Thivet, F., Knight, D., Zheltovodov, A., and Maksimov, A., "Insights in Turbulence Modeling for Crossing Shock Wave Boundary Layer Interactions", *AIAA Journal*, Vol. 39, No. 6, 2001, pp. 985-995.

Urbin, G., and Knight, D., "Large Eddy Simulation of a Supersonic Boundary Layer Using an Unstructured Grid", *AIAA Journal*, Vol. 39, No. 7, 2001, pp. 1288-1295.

Chernyavsky, B., and Knight, D., "Investigation of LES Code Scaling Performance and Network Type Influence on Linux PC Cluster", *International Journal of High Performance Computing Applications*, Vol. 15, No. 4, Winter 2001, pp. 388-393.

Thivet, F., Daouk, M., and Knight, D., "On the Wall Condition for the $k-\omega$ Turbulence Model", *AIAA Journal*, Vol. 40, No. 1, January 2002, pp. 179-181.

Thivet, F., Knight, D., Zheltovodov, A., and Maksimov, A., "Analysis of Observed and Computed Crossing Shock Wave Turbulent Boundary Layer Interactions", *Aerospace Science and Technology*, Vol. 6, No. 1, January 2002, pp. 3-17.

Yan, H., Knight, D. and Zheltovodov, A., "Large Eddy Simulation of Supersonic Flat Plate Boundary Layers Using the MILES Technique", *Journal of Fluid Engineering*, accepted.

Knight, D., Yan, H., Panaras, A. and Zheltovodov, A. A., "Advances in CFD Prediction of Shock Wave Turbulent Boundary Layer Interaction", *Progress in Aerospace Sciences*, to be submitted.

Conference Publications

Urbin, G., Knight, D., and Zheltovodov, A., "Compressible Large Eddy Simulation Using Unstructured Grids: Supersonic Turbulent Boundary Layer and Compression Corner", AIAA Paper No. 99-0427, January 1999.

Urbin, G., and Knight, D., "Compressible Large Eddy Simulation Using Unstructured Grid: Unstructured Boundary Layer", Second AFOSR Conference on DNS/LES, Rutgers University, June

7-9, 1999, Kluwer Academic Publishers, pp. 443-458.

Thivet, F., Knight, D., Zheltovodov, A., and Maksimov, A., "Improvement of Turbulence Modeling for Crossing Shock Wave Boundary Layer Interactions", AIAA Paper No. 2000-0131, January 2000.

Thivet, F., Besbes, O., and Knight, D., "How Far Should We Go to Get Mesh-Converged Skin-Friction and Heat-Transfer Coefficients?", AIAA Paper No. 2000-0820, January 2000.

Urbin, G., Knight, D., and Zheltovodov, A., "Large Eddy Simulation of Supersonic Compression Corner Part I", AIAA Paper No. 2000-0398, January 2000.

Chernyavsky, B., and Knight, D., "Comparison of CFD Code Performance on SGI Power Onyx and Pentium Cluster", International Conference on Parallel and Distributed Processing Techniques and Applications, June 2000.

Thivet, F., Knight, D., and Zheltovodov, A., "Computation of Crossing Shock Wave Boundary Layer Interactions with Realizable Two-Equation Turbulence Models", 10th International Conference on Methods of Aerophysical Research, Institute of Theoretical and Applied Mechanics, Russian Academy of Sciences, Novosibirsk, Russia, July 2000.

Yan, H., Urbin, G., Knight, D., and Zheltovodov, A., "Compressible Large Eddy Simulation Using Unstructured Grid: Supersonic Boundary Layer and Compression Ramps", 10th International Conference on Methods of Aerophysical Research, Institute of Theoretical and Applied Mechanics, Russian Academy of Sciences, Novosibirsk, Russia, July 2000.

Thivet, F., Knight, D., Zheltovodov, A., and Maksimov, A., "Numerical Prediction of Heat Transfer in Supersonic Inlets", ECCOMAS 2000, Barcelona, Spain, September 2000.

Chernyavsky, B., Yan, H., and Knight, D., "Analyses of Some Numerical Issues in Compressible LES", AIAA Paper No. 2001-0436, January 2001.

Thivet, F., Knight, D., Zheltovodov, A., and Maksimov, A., "Importance de la limitation des tension turbulentes pour la prévision des écoulements dans les prises d'air supersoniques", 37eme Colloque d'Aerodynamique Appliquee, 28-30 March 2001, Arcachon, France.

Thivet, F., Knight, D., Zheltovodov, A., and Maksimov, A., "Importance of Limiting the Turbulent Stresses to Predict 3D Shock-Wave Boundary-Layer Interactions", 23rd International Symposium on Shock Waves, Fort Worth, TX, July 2001.

Knight, D., Yan, H., and Zheltovodov, A., "Large Eddy Simulation of Supersonic Turbulent Flow in Expansion-Compression Corner", Third AFOSR International Conference on DNS and LES", University of Texas at Arlington, August 2001.

Yan, H., Knight, D., and Zheltovodov, A., "Large Eddy Simulation of Supersonic Compression Corner Using ENO Scheme", Third AFOSR International Conference on DNS and LES", University of Texas at Arlington, August 2001.

Zhou, X., and Knight, D., "Large Eddy Simulation of a Square Jet", Third AFOSR International Conference on DNS and LES", University of Texas at Arlington, August 2001.

Knight, D., "RTO WG 10: Test Cases for CFD Validation of Hypersonic Flight", AIAA Paper No. 2002-0433, January 2002.

Knight, D., Yan, H., Panaras, A. and Zheltovodov, A., "RTO WG 10: CFD Validation for Shock Wave Turbulent Boundary Layer Interactions", AIAA Paper No. 2002-0437, January 2002.

Knight, D., and Yan, H., "Large Eddy Simulation of Compressible Turbulent Flows", West East

High Speed Flowfield Conference, Marseilles, France, April 2002.

Yan, H., Knight, D. and Zheltovodov, A., "Large Eddy Simulation of Supersonic Flat Plate Boundary Layer Part II", AIAA/ASME/SAE/ASEE Joint Propulsion Conference & Exhibit, July 7-10, 2002

Bibliography

Abgrall, R. (1994) "On Essentially Non-oscillatory Schemes on Unstructured Meshes: Analysis and Implementation" *Journal of Computational Physics*, 114:45-58cp.

Adams, N. (1997) "Direct Numerical Simulation of Turbulent Supersonic Boundary Layer Flow", *Advances in DNS/LES - Proceedings of the First AFOSR International Conference on DNS/LES*, Greyden Press, Columbus, OH, pp 29-40, 1997.

Andreopoulos, J. and Muck, K. (1987) "Some New Aspects of the Shock-Wave Boundary Layer Interaction in Compression Ramp Flows", *Journal of Fluid Mechanics*, 180:405-428, 1987.

Ansari, A., and Strang, W. (1996) "Large-Eddy Simulation of Turbulent Mixing Layers", AIAA Paper No. 96-0684.

Bardina, J., Ferziger, J., and Reynolds, W. (1980) "Improved Subgrid Scale Model for Large Eddy Simulation", AIAA Paper No. 80-1357.

Barth, T. (1990) "On Unstructured Grids and Solvers", in *Computational Fluid Dynamics*, Lecture Notes 1990-03, von Karman Institute for Fluid Dynamics.

Barth, T. (1992) "Aspects of Unstructured Grids and Finite-Volume Solvers for the Euler and Navier-Stokes Equations", AGARD Special Course on Unstructured Grid Methods for Advection Dominated Flows, AGARD Report 787.

Boris, J., Grinstein, F., Oran, E., and Kolbe, R. (1992) "New Insights into Large Eddy Simulation" *Fluid Dynamics Research*, Vol. 10, pp. 199-228.

Comte-Bellot, G., and Corrsin, S. (1971) "Simple Eulerian Time Correlation of Full- and Narrow-Band Velocity Signals in Grid-Generated, Isotropic Turbulence", *Journal of Fluid Mechanics*, Vol. 48, Part 2, pp. 273-337.

David, E. (1993) "Modelisation des Ecoulements Compressibles et Hypersoniques : Une Approche Institutionnaire", *Ph.D Thesis*, Institut National Polytechnique de Grenoble, France, 1993.

Deardorff, J. (1970) "A Numerical Study of Three Dimensional Turbulent Channel Flow at Large Reynolds Numbers", *Journal of Fluid Mechanics*, Vol. 41, pp. 453-480.

Dolling, D. and Or, C. (1983) "Unsteadiness of the Shock Wave Structure in Attached and Separated Boundary Layers", AIAA Paper 83-1715, 1983.

Dussauge, J. and Gaviglio, J. (1987) "The Rapid Expansion of a Supersonic Turbulent Flow: Role of Bulk Dilatation", *Journal of Fluid Mechanics*, Vol. 174, pp. 81-112.

Eckelmann, H. (1974) "The Structure of the Viscous Sublayer and the Adjacent Wall Region in a Turbulent Channel Flow", *Journal of Fluid Mechanics*, 65:439-459, 1974.

El-Hady, N., Zang, T. and Piomelli, U. (1994) "Applications of the Dynamic Subgrid-Scale Model to Axisymmetric Transitional Boundary Layer at High Speed" *Physics of Fluids* Vol. 6, pp. 1299-1309.

Erlebacher, G., Hussaini, M., Speziale, C., and Zang, T. (1992) "Toward the Large-eddy Simulation of Compressible Turbulent Flows" *Journal of Fluid Mechanics* Vol. 238, pp. 155-185.

- Frink, N. (1994) "Recent Progress Toward a Three Dimensional Unstructured Navier-Stokes Flow Solver", AIAA Paper No. 94-0061, 1994.
- Galperin, B., and Orszag, S. (1993) "Large Eddy Simulation of Complex Engineering and Geophysical Flows", Cambridge University Press.
- Germano, M., Piomelli, U., Moin, P., and Cabot, W. (1991) "A Dynamic Subgrid-scale Eddy Viscosity Model", *Physics of Fluids A*, Vol. 3, pp. 1760-1765.
- Ghosal, S., Lund, T., Moin, P., and Akselvoll, K. (1995) "A Dynamical Localization Model for Large Eddy Simulation of Turbulent Flows", *Journal of Fluid Mechanics*, Vol. 286, pp. 229-255.
- Gottlieb, J., and Groth, C. (1988) "Assessment of Riemann Solvers for Unsteady One-Dimensional Inviscid Flows of Perfect Gases", *Journal of Computational Physics*, 78:437-458, 1988.
- Grinstein, F. F. and DeVore C. R. (1992) "Coherent Structure Dynamics in Spatially-Developing Square Jets", AIAA paper No. 92-3441.
- Grinstein, F. F., Gutmark, E. and Parr, T. (1995) "Near Field Dynamics of Subsonic Free Square Jets. A Computational and Experimental Study", *Physics of Fluids*, Vol. 7 no. 6, pp. 1483-1497.
- Grinstein, F. F. and Kailasanath, K. (1995) "Three-dimensional Numerical Simulations of Unsteady Reactive Square Jets", *Combustion and Flame*, Vol. 100, pp. 2-10.
- Grinstein, F. (1996) "Dynamics of Coherent Structures and Transition to Turbulence in Free Square Jets", AIAA Paper 96-0781.
- Grinstein, F. F. (2001) Vortex Dynamics and Entrainment in Rectangular Free Jets *J. Fluid Mech.*, Vol. 437, pp. 69-101
- Gutmark, E. J. and Grinstein, F. F. (1999) "Flow Control with Noncircular Jets" *Annu. Rev. Fluid Mech.*, Vol. 31, pp. 239-272
- Haworth, D., and Jansen, K. (1996) "Large Eddy Simulation on Unstructured Deforming Meshes: Towards Reciprocating IC Engines" Center for Turbulence Research, Stanford University and NASA Ames Research Center.
- C. Hirsh. (1997) "Numerical Computation of Internal and External Flows" Volume 2, John Wiley and Sons, reprinted March 1997.
- Hopkins, H. and Inouye, M. (1971) "An Evaluation of Theories for Predicting Skin Friction and Heat Transfer on Flat Plates at Supersonic and Hypersonic Mach Numbers", *AIAA Journal*, 9(6):993-1003, June 1971.
- Horstman, C. C. and Owen, F. K. (1972) "Turbulent Properties of a Compressible Boundary Layer", *AIAA Journal*, Vol. 10, No. 11, pp. 1418-1424.
- Horstman, C., Settles, G., Vas, I., Bogdonoff, S. and Hung, C. (1977) "Reynolds Number Effects on Shock Wave Turbulent Boundary Layer Interactions", *AIAA Journal*, 15:1152-1158, 1977.
- Hunt, D. and Nixon, D. (1995) "A Very Large Eddy Simulation of an Unsteady Shock Wave Turbulent Boundary Layer Interaction", AIAA Paper 95-2212, 1995.
- Jansen, K. (1997) "Large Eddy Simulation Using Unstructured Grids", in *First AFOSR International Conference on DNS/LES*, C. Liu and L. Sakell (editors), Louisiana Tech University, Ruston, Louisiana.
- Johnson, D. and Rose, W. (1975) "Laser Velocimeter and Hot Wire Anemometer Comparison in a

Supersonic Boundary Layer", *AIAA Journal*, 13:512-515, 1975.

Kim, J., Moin, P., and Moser, R. (1987) "Turbulence Statistics in Fully Developed Channel Flow at Low Reynolds Number", *Journal of Fluid Mechanics*, 177:133-166, 1987.

Knight, D. (1993) "Numerical Simulation of 3-D Shock Wave Turbulent Boundary Layer Interactions", AGARD/VKI Special Course on Shock- Wave Boundary-Layer Interactions in Supersonic and Hypersonic Flows, G. Degrez (editor), von Karman Institute for Fluid Dynamics, AGARD R-792, pp. 3-1 to 3-32.

Knight, D. (1994) "A Fully Implicit Navier-Stokes Algorithm Using an Unstructured Grid and Flux Difference Splitting", *Applied Numerical Mathematics*, 16:101-128, 1994.

Knight, D. (1997) "Numerical Simulation of Compressible Turbulent Flows Using the Reynolds-Averaged Navier-Stokes Equations", AGARD Special Course on Turbulence in Compressible Flows", AGARD Report R-819, 1997.

Knight, D., and Degrez, G. (1998) "Shock Wave Boundary Layer Interactions in High Mach Number Flows - A Critical Survey of Current Numerical Prediction Capabilities", AGARD Working Group 18 Report, to appear.

Knight, D., Zhou, G., Okong'o, N. and Shukla, V. (1998) "Compressible Large Eddy Simulation Using Unstructured Grids", AIAA Paper 98-0535, 1998.

Konrad, W. (1993) "A Three Dimensional Supersonic Turbulent Boundary Layer Generated by an Isentropic Compression", *Ph.D Thesis*, Princeton University, NJ, 1993.

Konrad, W. and Smits, A. (1998) "Turbulence Measurements in a Three-Dimensional Boundary Layer in Supersonic Flow", *Journal of Fluid Mechanics*, 372:1-23, 1998.

Kraichnan, R. (1976) "Eddy Viscosity in Two and Three Dimensions", *Journal of Atmospheric Sciences*, Vol. 33, pp. 1521-1536.

Kreplin, H. and Eckelmann, H. (1979) "Behavior of the Three Fluctuating Velocity Components in the Wall Region of a Turbulent Channel Flow", *Physics of Fluids*, 22(7):1233-1239, 1979.

Lesieur, M., and Métais, O. (1996) "New Trends in Large-Eddy Simulations of Turbulence" in *Annual Review of Fluid Mechanics*, Annual Reviews, Inc., Vol. 28, pp. 45-82.

Lilly, D. (1967) "The Presentation of Small-Scale Turbulent in Numerical Simulation Experiments", *IBM Scientific Computing Symposium on Environmental Sciences*, p. 195.

Lund, T., Wu, X. and Squires, K. (1998) "Generation of Turbulent Inflow Data for Spatially-Developing Boundary Layer Simulations", submitted to *Journal of Computational Physics*.

Mason, P. (1994) "Large Eddy Simulation: A Critical Review of the Technique" *Quarterly Journal of the Royal Meteorological Society* Vol. 120, pp. 1-26.

Meier, H. U. and Rotta, J. C. (1971) "Temperature Distributions in Supersonic Turbulent Boundary Layer" *AIAA Journal*, Vol. 9, No. 11, pp. 2149-2156.

Menon, S., and Kim, W.-W. (1996) "High Reynolds Numerical Flow Simulation Using the Localized Dynamic Subgrid-Scale Model", AIAA Paper No. 96-0425.

Moin, P., Squires, K., Cabot, W., and Lee, S. (1991) "A Dynamic Subgrid-scale Model for Compressible Turbulence and Scalar Transport", *Physics of Fluids A*, Vol. 11, pp. 2746-2757.

Moin, P. (1997) "Progress in Large Eddy Simulation of Turbulent Flows", AIAA Paper 97-0749.

- Muck, K., Spina, E., Smits, A. (1984) "Compilation of Turbulence Data for an 8 degree Compression Corner at Mach 2.9", Report MAE-1642, April 1984.
- Muck, K., Dussauge, J., Bogdonoff, S. (1985) "Structure of Wall Pressure Fluctuations in a Shock-Induced Separated Flow", AIAA Paper No. 85-0179, 1985.
- Okong'o, N. and Knight, D. (1998) "Compressible Large Eddy Simulation Using Unstructured Grids: Channel and Boundary Layer Flows", AIAA Paper 98-3315, 1998.
- Ollivier-Gooch, C. F. (1997) "High Order ENO Schemes for Unstructured Meshes Based on Least Squares Reconstruction, AIAA Paper No. 97-0540, 1997.
- Oran, E., and Boris, J. (1993) "Computing Turbulent Shear Flows - A Convenient Conspiracy" *Computers in Physics* Vol. 7, No. 5, pp. 523-533.
- Panchapakesan, N. R. and Lumley, J. L. (1993) "Turbulence Measurements in Axisymmetric Jets of Air and Helium. Part 1. Air Jet" *J. Fluid Mech.*, Vol. 246, pp. 197-223.
- Piomelli, U., Cabot, W., Moin, P., and Lee, S. (1991) "Subgrid Scale Backscatter in Turbulent and Transitional Flows", *Physics of Fluids A*, Vol. 3, pp. 1766-1771.
- Porter, D., Pouquet, A., and Woodward, P. (1994) "Kolmogorov-like Spectra in Decaying Three-Dimensional Supersonic Flows", *Physics of Fluids* Vol. 6, No. 6, pp. 2133-2142.
- Rodi, W. (1980) "Turbulence Models and Their Application in Hydraulics-A State of the Art Review" IAHR, Delft.
- Settles, G., Fitzpatrick, T., and Bogdonoff, S. (1979) "Detailed Study of Attached and Separated Compression Corner Flowfields in High Reynolds Number Supersonic Flow", *AIAA Journal*, 17:579-585, 1979.
- Simpson, R. L., Whitten, D. G. and Moffat, R. J. (1970) "An Experimental Study of the Turbulent Prandtl Number of Air with Injection and Suction", *Int. Journal of Heat Transfer*, Vol. 13, pp. 125-143, 1970.
- Smagorinsky, J. (1963) "General Circulation Experiments with the Primitive Equations, I. The Basic Experiment", *Monthly Weather Review*, Vol. 91, pp. 99-164.
- Smits, A. and Muck, K. (1987) "Experimental Study of Three Shock Wave / Turbulent Boundary Layer Interactions", *Journal of Fluid Mechanics*, 182:291-314, September 1987.
- Smits, A. and Dussauge, J.-P. (1996) *Turbulent Shear Layers in Supersonic Flow*, American Institute of Physics, New York, 1996.
- Speziale, C., Erlebacher, G., Zang, A., and Hussaini, M. (1988) "The Subgrid Modeling of Compressible Turbulence" *Physics of Fluids*, Vol. 31, No. 4, pp. 940-943.
- Spyropoulos, E., and Blaisdell, G. (1996) "Evaluation of the Dynamic Model for Simulations of Compressible Decaying Isotropic Turbulence", *AIAA Journal* Vol. 34, No. 5, pp. 990-998.
- Stephen, A. and Mo, S. and Gregory, S. (1998) "The Effects of Expansion on the Turbulence Structure of Compressible Boundary Layers", *J. Fluid Mechanics*, Vol. 367, pp 67-105.
- Urbin, G., Knight, D. and Zheltovodov, A. A. (1999) "Compressible Large Eddy Simulation using Unstructured Grid: Supersonic Turbulent Boundary Layer and Compression Corner", *AIAA Paper 99-0427*
- Urbin, G. and Knight, D. (2001) "Large Eddy Simulation of a Supersonic Boundary Layer Using

an Unstructured Grid", *AIAA Journal*, Vol.39, No. 8, pp. 1288-1295.

Walz, A. (1969) *Boundary Layers of Flow and Temperature*, MIT Press, Cambridge, 1969.

Yoshizawa, A. (1986) "Statistical Theory for Compressible Turbulent Shear Flows, with the Application to Subgrid Modeling" *Physics of Fluids*, Vol. 29, pp. 2152-2164.

Zang, T., Dahlburg, R. and Dahlburg, P. (1992) "Direct and Large Eddy Simulations of Three-Dimensional Compressible Navier-Stokes Turbulence" *Physics of Fluids A*, Vol. 4, No. 1, pp. 127-140.

Zhelтоводов, A., Schuelein, A., and Yakovlev, V. (1983) "Turbulent Boundary Layer Development Under Conditions of Mixed Interaction with Shocks and Expansion Waves", Preprint No 28-83, Institute of Theoretical and Applied Mechanics, USSR Acad. of Sciences, Novosibirsk, 1983, 51 pg. (in Russian).

Zhelтоводов, A., and Yakovlev, V. (1984) "Turbulence Study in Compressible Unseparated and Separated Flows", Report No 1418, Institute of Theoretical and Applied Mechanics, USSR Academy of Sciences, Novosibirsk 1984, 100 pg. (in Russian).

Zhelтоводов, A. and Yakovlev, V. (1986) "Stages of Development, Gas Dynamic Structure and Turbulence Characteristics of Turbulent Compressible Separated Flows in the Vicinity of 2-D Obstacles", Preprint No 27-86, Institute of Theoretical and Applied Mechanics, USSR Academy of Sciences, Novosibirsk, 1986, 55 pg. (in Russian).

Zhelтоводов, A. A. and Schuelein, E. (1987) "The Peculiarities of Turbulent Separation Development in Disturbed Boundary Layers", *Modeling in Mechanics*, Vol. 2, No. 1, pp. 53-58 (in Russian)

Zhelтоводов, A. A. and Mecler, L. and Schuelein, E. (1987) "Peculiarities of Development of Separated Flows in Compression Corners After the Expansion Fans", ITAM Preprint 10-87 (In Russian)

Zhelтоводов, A., Trofimov, V., Shilein, E., and Yakovlev, V. (1990) "An Experimental Investigation of Supersonic Turbulent Flows in the Vicinity of Sloping Forward and Back Facing Step", Report No 2030, Inst. of Theoretical and Applied Mechanics, USSR Academy of Sciences, Novosibirsk, 1990.

A. Zheltovodov and V. Trofimov and E. Filippova and Y. Takovlev (1990a) "Influence of Turbulence Change on the Heat Exchange Under the Conditions of Supersonic Separated Flows", *Abstracts: IUTAM Symposium on Separated Flows and Jets*, pp. 273-274, USSR Academy of Sciences, Siberian Division, Novosibirsk.

Zhelтоводов, A. and Borisov, A. and Knight, D. and Horstman, C. and Settles, G. (1992) "The Possibilities of Numerical Simulation of Shock Waves / Boundary Layer Interaction in Supersonic and Hypersonic Flows", *Proceedings of the International Conference on Methods of Aerophysical Research. Part 1*, "Russian Academy of Sciences, Siberian Division, Novosibirsk", pp. 164-170.

Zhelтоводов, A. A. and Horstman, C. C. (1993) "Experimental and Numerical Investigation of 2-D Expansion/Shock Wave - Turbulent Boundary Layer Interaction", *Preprint No 2-93, Institute of Theoretical and Applied Mechanics, Russian Academy of Sciences, Novosibirsk*

Zhelтоводов, A. (1996) "Shock Waves / Turbulent Boundary Layer Interactions - Fundamental Studies and Applications", *AIAA Paper 96-1977*, 1996.

Zukoski, E. E. (1967) "Turbulent Boundary Layer Separation in front of a Forward Facing Step", *AIAA J.*, Vol. 5, No. 10, pp. 1746-1753.